

Decoherence and decay of motional quantum states of a trapped atom coupled to engineered reservoirs*

Q.A. Turchette**, C.J. Myatt***, B.E. King****, C.A. Sackett, D. Kielpinski,
W.M. Itano, C. Monroe, and D.J. Wineland

*Time and Frequency Division, National Institute of Standards and Technology, Boulder, Colorado
80303*

We present results from an experimental study of the decoherence and decay of quantum states of a trapped atomic ion's harmonic motion interacting with several types of *engineered* reservoirs. We experimentally simulate three types of reservoirs: a high-temperature amplitude reservoir, a zero-temperature amplitude reservoir, and a high-temperature phase reservoir. Interaction with these environments causes the ion's motional state to decay or heat, and in the case of superposition states, to lose coherence. We report measurements of the decoherence of superpositions of coherent states and two-Fock-state superpositions into these reservoirs, as well as the decay and heating of Fock states. We confirm the theoretically well-known scaling laws that predict that the decoherence rate of superposition states scales with the square of the “size” of the state.

I. INTRODUCTION

The decoherence and decay of quantum states coupled to a variety of reservoirs have been investigated extensively in theory [1–8]. The model in these studies is typically a system harmonic oscillator coupled to a bath of environment harmonic oscillators. One of the most interesting results has been the realization that macroscopic superposition states decay at extremely fast rates. As an illustration, consider a charged harmonic oscillator system in a superposition of coherent states $\psi \propto |\alpha_1\rangle + |\alpha_2\rangle$ coupled to the noisy electric field \mathbf{E} of the environment. The interaction potential is $V = -q\mathbf{x} \cdot \mathbf{E}$, where \mathbf{x} is the position and q is the charge of the particle. Regardless of the temperature of the reservoir, $\langle \mathbf{E}^2 \rangle \neq 0$, so that the system is always subject to some level of noise from the environment. For a superposition of coherent states coupled to a reservoir of fluctuating fields, a simple scaling law may be stated [3]: the rate of decoherence scales as the square of the separation of the wave packets, $|\Delta\alpha|^2 = |\alpha_1 - \alpha_2|^2$. In an idealized case, the superposition is created, the amplitude reservoir is coupled to the system for a time t , and the coupling is then turned off. The remaining coherence C between the two wave packets, expressed for instance as the magnitude of the off-diagonal components of the system density matrix, is

$$C(t) = C(0) \exp \left[-|\Delta\alpha|^2 \frac{\gamma}{2} t \right], \quad (1)$$

where γ is a coupling constant between the reservoir and the system. For the same interaction, the energy H of the system decays like

$$H(t) = H(0) \exp [-\gamma t], \quad (2)$$

at a rate independent of the size of the initial state. For superpositions of macroscopic-sized wavepackets, the quantum coherence may be obliterated in a time over which the energy of the system does not change appreciably.

Significant attention has been paid to the role of decoherence in the classical/quantum correspondence and in fundamental issues of physics. Recently, decoherence has also been studied in a more pragmatic role: as a primary impediment to quantum computing. Quantum computation relies on entanglement of large quantum states to perform efficient calculations. Such states, separated by large distances in Hilbert space, will be very susceptible to the detrimental effects of decoherence. Any system will interact with its environment, so the nature of the interaction and the time scales over which it acts are of critical import in implementations of quantum information processing. Since trapped ions are a leading technology for investigations in quantum computing, a study of decoherence in an ion trap quantum computer system [9], as presented here, is particularly relevant.

Over the past several years, techniques have been described to generate mesoscopic superpositions, called “Schrödinger cats,” of motional states of trapped ions [10] and of photon states in cavity quantum electrodynamics [11]. In both cases decoherence through coupling to ambient reservoirs was observed, and sensitivity to the size of the superposition was demonstrated [10,11]. In more recent work with trapped ions [12], we extended the investigations beyond ambient reservoirs and “engineered” the form, bandwidth and strength of coupling to the reservoir. We observed for the first time the quantitative scaling laws of the decoherence of superpositions of coherent states and superpositions of Fock states into a variety of reservoirs for a range of parameters. This article is a more detailed discussion of the experiments of Ref. [12] with additional theoretical development and additional data.

The article is arranged as follows. In Section II we review the theory of the damping of a harmonic oscillator coupled to several types of reservoirs. In particular, we derive specific formulae for the time evolution of the density matrix for several types of system-reservoir interactions. In section III we discuss the experimental apparatus and techniques, and in Section IV we analyze the data.

II. THEORETICAL SUMMARY

A. Damping of harmonic oscillators

1. Thermal amplitude reservoir

We begin by reminding the reader of some formal results in the theory of damping of harmonic oscillators coupled to two types of baths. In this section we consider the case in which the reservoir is a bath of oscillators, and the coupling is to the position of the oscillator via the interaction Hamiltonian

$$H_I = \hbar \sum_i \left(\Gamma_i \hat{b}_i \hat{a}^\dagger + \Gamma_i^* \hat{b}_i^\dagger \hat{a} \right). \quad (3)$$

where Γ_i is the coupling rate of the i^{th} bath oscillator to the system, \hat{b}_i is the lowering operator of this reservoir oscillator and \hat{a} is the lowering operator of the system oscillator. This is known as an amplitude coupling. If furthermore, the reservoir oscillators are in

thermal equilibrium at temperature T , then the system exchanges energy with the reservoir in a process leading to overall thermal equilibrium. The time evolution of this process is described by the following master equation for the system density matrix formed by tracing over the reservoir degrees of freedom [5]:

$$\dot{\rho}(t) = \frac{\gamma}{2} (\bar{n} + 1) (2\hat{a}\rho\hat{a}^\dagger - \hat{a}^\dagger\hat{a}\rho - \rho\hat{a}^\dagger\hat{a}) + \frac{\gamma}{2}\bar{n} (2\hat{a}^\dagger\rho\hat{a} - \hat{a}\hat{a}^\dagger\rho - \rho\hat{a}\hat{a}^\dagger). \quad (4)$$

where γ is the system decay rate and \bar{n} is the average number of quanta in the reservoir at the resonance frequency of the system oscillator ω_0 :

$$\bar{n} = \frac{e^{-\hbar\omega_0/k_B T}}{1 - e^{-\hbar\omega_0/k_B T}} \quad (5)$$

and k_B is Boltzmann's constant. The zero-temperature reservoir ($\bar{n} = 0$) is a special case of the thermal amplitude reservoir in which the inescapable quantum noise dominates the classical thermal noise of fluctuating oscillators.

a. Amplitude damping, Fock states The solution of Eq. 4 is non-trivial, and has been discussed at some length in the literature (which is reviewed in Ref. [8]). We first consider its solution in a Fock-state basis. In this basis, the decomposition of $\rho(t)$ is given by:

$$\rho(t) = \sum_{n,m} \rho_{nm}(t) |n\rangle\langle m|. \quad (6)$$

Based on calculations presented in Ref. [13], we state the solution to Eq. 4 with the expansion of Eq. 6 as:

$$\begin{aligned} \rho_{nm}(t) = & \frac{1}{1 + N(t)} \sum_{j=0}^{\min(n,m)} \left(\frac{N(t)}{1 + N(t)} \right)^j \left(\frac{e^{\gamma t/2}}{1 + N(t)} \right)^{n+m-2j} \times \\ & \sum_{l=0}^{\infty} \left(1 - \frac{e^{-\gamma t}}{1 + N(t)} \right)^l \times \\ & \sqrt{\binom{n+l-j}{n-j} \binom{m+l-j}{m-j} \binom{n}{j} \binom{m}{j}} \rho_{n+l-j, m+l-j}(0), \end{aligned} \quad (7)$$

where $\rho_{nm}(0)$ is the initial density matrix and

$$N(t) = \bar{n}(1 - e^{-\gamma t}) \quad (8)$$

can be interpreted as the average number of quanta in the *system* at time t for an initial ground state system ($\rho(0) = |0\rangle\langle 0|$). The form of Eq. 7 is qualitatively illuminating: the evolution of a given density matrix element depends only on neighbors along its own diagonal. We note that this calculation has been performed in Refs. [13,14]. We used Ref. [13] to derive Eq. 7; in this reference the final form (Ref. [13], Eq. 37) seems to be written incorrectly, though the correct result can be derived from earlier equations. In Ref. [14] the result is written in terms of the Q -function, and agrees with Ref. [13], and therefore not with our result.

In some cases, we are interested in the time-evolution of the diagonal elements only, which are given by:

$$\rho_{nn}(t) = \frac{1}{1+N(t)} \sum_{j=0}^n \left(\frac{N(t)}{1+N(t)} \right)^j \left(\frac{e^{-\gamma t/2}}{1+N(t)} \right)^{2n-2j} \quad (9)$$

$$\times \sum_{l=0}^{\infty} \left(1 - \frac{e^{-\gamma t}}{1+N(t)} \right)^l \binom{n+l-j}{n-j} \binom{n}{j} \rho_{n+l-j, n+l-j}(0). \quad (10)$$

As stated above, the zero-temperature reservoir is a special case of the amplitude reservoir. We write the solution in this case as:

$$\rho_{nm}(t) = e^{-(n+m)\gamma t/2} \sum_{l=0}^{\infty} \left(1 - e^{-\gamma t} \right)^l \sqrt{\binom{n+l}{n} \binom{m+l}{m}} \rho_{n+l, m+l}(0). \quad (11)$$

For the diagonals only,

$$\rho_{nn}(t) = e^{-n\gamma t} \sum_{l=0}^{\infty} \left(1 - e^{-\gamma t} \right)^l \binom{n+l}{n} \rho_{n+l, n+l}(0). \quad (12)$$

b. Amplitude damping, coherent states In this paragraph we consider the solution of Eq. 4 in a situation appropriate to coherent state evolution. We follow exactly the results of Ref. [4]. For coherent states the density matrix is expanded as:

$$\rho(t) = \int d^2\mu d^2\nu P(\mu, \nu^*) \frac{|\nu\rangle\langle\mu|}{\langle\nu|\mu\rangle}, \quad (13)$$

where $P(\mu, \nu^*)$ is the positive-P representation [5–7]. The solution to Eq. 4 is written [4]

$$\rho(t) = \int d^2\mu d^2\nu P_0(\mu, \nu^*) \langle\nu|\mu\rangle^{\frac{-e^{-\gamma t}}{1+2N(t)}} \hat{\mathcal{D}}(\bar{\mu}) \rho_T(t) \hat{\mathcal{D}}^\dagger(\bar{\nu}) \quad (14)$$

where $P_0(\mu, \nu^*)$ describes the initial system density matrix through Eq. 13,

$$\bar{\mu} = \frac{e^{-\gamma t/2}}{1+2N(t)} [(1+N(t))\mu + N(t)\nu], \quad (15)$$

$$\bar{\nu} = \frac{e^{-\gamma t/2}}{1+2N(t)} [(1+N(t))\nu + N(t)\mu], \quad (16)$$

and $\rho_T(t)$ is a thermal state density matrix with $N(t)$ quanta:

$$\rho_T(t) = \frac{1}{1+N(t)} \sum_m \left[\frac{N(t)}{1+N(t)} \right]^m |m\rangle\langle m|. \quad (17)$$

$N(t)$ is defined in Eq. 8. $\hat{\mathcal{D}}$ is the displacement operator $\hat{\mathcal{D}}(\alpha)|0\rangle = |\alpha\rangle$. The form of this solution makes it difficult to see the simple result for the off-diagonal elements of the density matrix as presented in the introduction. The appropriate experimental measurement will reveal it when we apply this formal result below.

2. Phase reservoir

Here we consider a reservoir whose coupling preserves the energy of the system, with interaction Hamiltonian

$$H_I = \hbar \sum_i \left(\Gamma_i \hat{b}_i \hat{a}^\dagger \hat{a} + \Gamma_i^* \hat{b}_i^\dagger \hat{a}^\dagger \hat{a} \right). \quad (18)$$

This is known as a phase-damping reservoir.

For the system-reservoir interaction described by Eq. 18 and a reservoir in thermal equilibrium at a temperature corresponding to a mean occupation number \bar{n} (as in Eq. 5), the master equation is given by [6]:

$$\dot{\rho}(t) = \frac{\kappa}{2} \left(2\hat{a}^\dagger \hat{a} \rho \hat{a}^\dagger \hat{a} - (\hat{a}^\dagger \hat{a})^2 \rho - \rho (\hat{a}^\dagger \hat{a})^2 \right). \quad (19)$$

Here $\kappa = K(2\bar{n} + 1)$, is the system decay rate with K the coupling to the reservoir of oscillators.

a. Phase damping, Fock states For initial Fock states, the solution of Eq. 19 is straightforward. Using the expansion of Eq. 6,

$$\dot{\rho}_{nm} = -\frac{\kappa}{2}(n - m)^2 \rho_{nm}, \quad (20)$$

with solution

$$\rho_{nm}(t) = e^{-\frac{\kappa}{2}(n-m)^2 t} \rho_{nm}(0). \quad (21)$$

Here it is clear that the off-diagonal density matrix elements decay exponentially at a rate proportional to the square of their distance from the diagonal.

b. Phase damping, coherent states For the coherent state basis, the solution of Eq. 19 is rather complicated. We will forego its solution in favor of the technique presented in the next section.

B. Interferometry

This section presents an experimentally motivated approach to calculating the decay of quantum coherences. Here the off-diagonal matrix elements are measured as the contrast of an ion interferometry experiment. This section is adapted from Ref. [15].

1. Ion states and transitions

First we review a few details necessary to understand the ion interferometer analysis. For the purposes of this section, a trapped ion has an external degree of freedom that is a perfect 1-D harmonic oscillator (along \hat{z}) of frequency ω . The internal degree of freedom is assumed to be a perfect two-state system, the states of which we label in analogy with a spin-1/2 system by $|\downarrow\rangle$ and $|\uparrow\rangle$. The states $|\downarrow\rangle$ and $|\uparrow\rangle$ are coupled to the motional harmonic oscillator states $|n\rangle$ via a classical optical laser field. The interaction Hamiltonian

has resonant couplings between internal states $|s\rangle$ ($|s\rangle = |\downarrow\rangle$ or $|\uparrow\rangle$) and motional states $|n\rangle$ whose matrix elements are [16,17]

$$\langle s', n' | \hat{H}_I | s, n \rangle = \hbar \Omega \langle s', n' | \sigma_+ e^{i\eta(\hat{a} + \hat{a}^\dagger)} + \sigma_- e^{-i\eta(\hat{a} + \hat{a}^\dagger)} | s, n \rangle, \quad (22)$$

where σ_+ (σ_-) is the atomic raising (lowering) operator, \hat{a}^\dagger (\hat{a}) is the harmonic oscillator creation (annihilation) operator, Ω is the laser-atom coupling strength, or Rabi frequency and $\eta = \delta k z_0$ is the Lamb-Dicke parameter, where δk is the \hat{z} component of the applied field wave-vector and $z_0 = \sqrt{\hbar/2m\omega}$ is the harmonic oscillator characteristic length [16].

The excitation spectrum of the ion consists of a carrier transition ($|\downarrow\rangle|n\rangle \leftrightarrow |\uparrow\rangle|n\rangle$) and motional sideband transitions ($|\downarrow\rangle|n\rangle \leftrightarrow |\uparrow\rangle|m\rangle$ $n \neq m$). The sideband transition frequencies differ from that of the carrier by a frequency of $(n-m)\omega$, where $|n-m|$ is the order (first, second, etc.) of the sideband. With resolved sideband cooling [18] and optical pumping we prepare the ion in the $|\downarrow\rangle|0\rangle$ state before each repetition of the experiment.

At the end of any experiment, there is one observable: the probability that the ion is found in the $|\downarrow\rangle$ state, denoted by P_\downarrow . The measurement is not sensitive to the motional state of the ion, so a trace over the motion is required to calculate this probability. The final density matrix at the end of an experiment is written ρ_f , and in general is not separable between spin and motion parts. The detection signal is given by

$$P_\downarrow = \langle \downarrow | \text{Tr}_M \rho_f | \downarrow \rangle = \sum_n \langle n | \langle \downarrow | \rho_f | \downarrow \rangle | n \rangle. \quad (23)$$

For pure states $\rho_f = |\psi_f\rangle\langle\psi_f|$ this reduces to

$$P_\downarrow = \sum_n |\langle \downarrow | \langle n | \psi_f \rangle|^2. \quad (24)$$

In experiments in which a coherence is measured, we employ a type of Ramsey interferometry. Generically, the procedure is to embed the coupling to the reservoir between the initial and final “beamsplitters” of a Ramsey interferometer. The beamsplitters create and undo a motional quantum state. As the coherence of the quantum state is degraded (due to interaction with the reservoir) the contrast of the Ramsey fringes decreases, giving a measure of the remaining coherence.

2. Amplitude reservoirs

a. Schrödinger cat interferometer and amplitude reservoir The first type of interferometer that we employ uses the Schrödinger cat state [10]

$$|\psi\rangle = \frac{1}{\sqrt{2}} (|\downarrow\rangle|\alpha_\downarrow\rangle + |\uparrow\rangle|\alpha_\uparrow\rangle) \quad (25)$$

where $|\uparrow\rangle$ and $|\downarrow\rangle$ are internal states of the ion, and $|\alpha_{\downarrow,\uparrow}\rangle$ are coherent states of the ion’s motion in the harmonic well of the trap. As will be seen, the action of an amplitude reservoir on this Schrödinger cat interferometer clearly illustrates the scaling of the decoherence as a function of the size of the superposition.

A diagram of the Schrödinger cat interferometer is presented in Figure 1. Initially the ion is prepared in the state $|\psi\rangle = |\downarrow\rangle|0\rangle$. Next, we generate the spin superposition $|\psi\rangle = (|\downarrow\rangle + |\uparrow\rangle)|0\rangle/\sqrt{2}$, as shown in panel 1. The motional superposition is created by applying a spin-dependent optical dipole force that approximates the coherent displacement operators [10,19] $\mathcal{D}(\alpha_\downarrow)$ and $\mathcal{D}(\alpha_\uparrow)$ acting on the states $|\downarrow\rangle$ and $|\uparrow\rangle$. The resulting state (with constant phase factors suppressed), shown in panel 2, is that of Eq. 25. These two operations constitute the first “beam splitter”, or Ramsey zone of the interferometer. During the Ramsey waiting time, the amplitude reservoir (with coupling shown in Eq. 3) is applied, by placing noisy fields on the trap electrodes (this will be discussed in Section III C 1 below). The application of the amplitude reservoir for a fixed time results in a random displacement β that displaces both spin states equally. Since

$$\mathcal{D}(\lambda)|\kappa\rangle = e^{-i\text{Im}[\lambda^*\kappa]}|\lambda + \kappa\rangle, \quad (26)$$

where $|\kappa\rangle$ and $|\lambda + \kappa\rangle$ are coherent states, after application of the operator $\mathcal{D}(\beta)$ to the wavefunction from Eq. 25

$$|\psi\rangle = \frac{1}{\sqrt{2}} \left(|\downarrow\rangle|\alpha_\downarrow + \beta\rangle + e^{i\text{Im}[\beta\Delta\alpha^*]}|\uparrow\rangle|\alpha_\uparrow + \beta\rangle \right), \quad (27)$$

where $\Delta\alpha = \alpha_\uparrow - \alpha_\downarrow$ and an overall phase factor has been removed. The motional superposition is reversed by applying $\mathcal{D}(-\alpha_\downarrow)$ and $\mathcal{D}(-\alpha_\uparrow)$, resulting in

$$|\psi\rangle = \frac{1}{\sqrt{2}} \left(|\downarrow\rangle + e^{2i\text{Im}[\beta\Delta\alpha^*]}|\uparrow\rangle \right) |\beta\rangle. \quad (28)$$

A final $\pi/2$ pulse transforms the spins as

$$|\downarrow\rangle \longrightarrow \frac{1}{\sqrt{2}} \left(|\downarrow\rangle + e^{-i\delta}|\uparrow\rangle \right) \quad (29)$$

$$|\uparrow\rangle \longrightarrow \frac{1}{\sqrt{2}} \left(|\uparrow\rangle - e^{i\delta}|\downarrow\rangle \right), \quad (30)$$

and yields the state

$$|\psi\rangle = \frac{1}{2} \left[\left(1 + e^{i(\delta + 2\text{Im}[\beta\Delta\alpha^*])} \right) |\downarrow\rangle + \left(e^{2i\text{Im}[\beta\Delta\alpha^*]} - e^{i\delta} \right) |\uparrow\rangle \right] |\beta\rangle, \quad (31)$$

where δ is the Ramsey phase, i.e., the phase difference between the initial and final $\pi/2$ spin flips. These last two steps constitute the second, recombining beam splitter of the interferometer.

In a single experiment the probability that the ion is in the $|\downarrow\rangle$ state is

$$P_\downarrow(\beta) = |\langle\downarrow|\psi\rangle|^2 = \frac{1}{2} \left[1 + \cos \left(\delta + 2\text{Im}[\beta\Delta\alpha^*] \right) \right]. \quad (32)$$

If β were fixed on each repetition of the experiment, as the Ramsey phase δ is swept, the signal would be a perfect cosine with phase dictated by the displacement β . The decoherence (and loss of contrast in this picture) enters, because β is a random variable that fluctuates to a different value on each repetition of the experiment, giving rise to a random phase shift

of the fringe which averages the contrast away from unity. In the experiment, we force β to be a Gaussian distributed random variable, as, for example, realized by a hot resistor coupled to the trap electrodes. We take both $\text{Re } \beta$ and $\text{Im } \beta$ to have a standard deviation σ . An ensemble average of $P_{\downarrow}(\beta)$ yields the form of the Ramsey fringes:

$$P_{\downarrow} = \frac{1}{2} \left[1 + e^{-2|\Delta\alpha|^2\sigma^2} \cos \delta \right]. \quad (33)$$

We see that the contrast of the fringes is exponentially sensitive to (the square of) the “size” $|\Delta\alpha|$ of the superposition. This scaling [3,7,20] is one of the key results that is demonstrated experimentally in a later section.

b. Fock state interferometer and amplitude reservoir A second type of interferometer generates a superposition of two Fock states with the first beamsplitter using the technique described in Ref. [17]. For example, consider the interferometer that generates the superposition $(|0\rangle + |2\rangle)/\sqrt{2}$ and then recombines the two parts of the wavefunction to produce interference fringes. Starting from the state $|\downarrow\rangle|0\rangle$, a $\pi/2$ pulse on the first blue sideband generates the state $|\psi\rangle = (|\downarrow\rangle|0\rangle + |\uparrow\rangle|1\rangle)/\sqrt{2}$. A π pulse tuned to the first red sideband drives the transition $|\uparrow\rangle|1\rangle \rightarrow |\downarrow\rangle|2\rangle$ while leaving the population in the $|\downarrow\rangle|0\rangle$ state unperturbed. This combination of pulses generates the superposition

$$|\psi\rangle = \frac{1}{\sqrt{2}} |\downarrow\rangle (|0\rangle + |2\rangle). \quad (34)$$

The second beamsplitter of the interferometer is realized by reversing the above procedure—driving a $-\pi$ pulse on the first red sideband followed by a $\pi/2$ pulse on the first blue sideband. When the phase of the second $\pi/2$ pulse is swept, the spin state at the end of the experiment oscillates between $|\downarrow\rangle$ and $|\uparrow\rangle$.

For the experiments reported here, we use two pulses to generate the beam splitters in the Fock state interferometer. For the first beamsplitter, the first pulse is a $\pi/2$ pulse on the n' th order blue sideband, generating the state

$$|\psi\rangle = \frac{1}{\sqrt{2}} (|\downarrow\rangle|0\rangle + |\uparrow\rangle|n'\rangle). \quad (35)$$

A second pulse selectively drives only one of the spin components, resulting in the Fock state superposition

$$|\psi\rangle = \frac{1}{\sqrt{2}} |s\rangle (|m\rangle + |n\rangle), \quad (36)$$

where $|s\rangle$ denotes one of the spin states $|\downarrow\rangle$ or $|\uparrow\rangle$. The four pairs of Fock states generated in the experiments, along with the pulses used to generate the superpositions, are shown in Table I.

The Fock state interferometer can be coupled to an amplitude reservoir. For simplicity, we restrict ourselves to Fock state superpositions of the form

$$|\psi\rangle = \frac{1}{\sqrt{2}} |\downarrow\rangle (|0\rangle + |m\rangle). \quad (37)$$

It is an extended exercise to calculate results for the entire interferometer in the manner of the preceding case (coherent states in amplitude reservoir). The complication is twofold: First, displacing Fock states leads to cumbersome expressions. Second, there is a problem with the beamsplitters: the pulses of the second beam splitter are π and $\pi/2$ pulses strictly for the transitions $|\downarrow\rangle|m\rangle \leftrightarrow |\uparrow\rangle|m-1\rangle$ and $|\downarrow\rangle|0\rangle \leftrightarrow |\uparrow\rangle|m-1\rangle$, respectively. Thus applying these pulses to an ion in a motional state which has decayed away from its original form does not result in full interference. It turns out that while the calculation is complicated, the details are not important to the actual experiment, which is performed only for small m , and in the limit $\gamma t \ll 1$. Rather than present the full calculation, we will merely state a simple result based on the master equation approach. For states of the type shown in Eq. 37, the time-evolution of the relevant density matrix elements predicted by Eq. 7 reduces to the simple form

$$\rho_{0,m} \approx \frac{1}{2(1 + \bar{n}\gamma t)^{1+m}} \quad (38)$$

for $\gamma t \ll 1$. The measured contrast is simply twice this matrix element. For the range of m and $\bar{n}\gamma t$ studied in the experiment, this expression differs by less than 5% from an exact treatment of the imperfect interference.

3. phase reservoirs

a. Schrödinger cat interferometer and phase reservoir A second reservoir that we apply is a phase reservoir. A phase reservoir is realized by adiabatically changing the trap frequency for a period of time and then restoring the original trap frequency. If the deviation of the trap frequency is $\delta\omega(t)$, then the phase shift of the ion oscillation in time T is

$$\phi = \int_0^T \delta\omega(t) dt. \quad (39)$$

The potentials required to change the trap frequency are applied to the trap electrodes during the Ramsey time between the beamsplitter pulses (see Section III C 2).

The effect of a phase reservoir on a Schrödinger cat state is diagrammed in Figure 2. The generation of the Schrödinger cat state $|\psi\rangle = (|\downarrow\rangle|\alpha_\downarrow\rangle + |\uparrow\rangle|\alpha_\uparrow\rangle) / \sqrt{2}$ is accomplished as discussed previously. A phase shift of the ion oscillation by the random variable ϕ introduces complex phase factors to the coherent states,

$$|\psi\rangle = \frac{1}{\sqrt{2}} \left(|\downarrow\rangle|\alpha_\downarrow e^{i\phi}\rangle + |\uparrow\rangle|\alpha_\uparrow e^{i\phi}\rangle \right). \quad (40)$$

Due to these phase factors $e^{i\phi}$, the motional superposition is not correctly reversed, as shown in Figure 2, panel 4. The second beamsplitter consists of the displacements $\mathcal{D}(-\alpha_\downarrow)$ and $\mathcal{D}(-\alpha_\uparrow)$ followed by a second $\pi/2$ pulse on the carrier, yielding

$$\begin{aligned} |\psi\rangle = \frac{1}{2} \Big[& e^{i|\alpha_\downarrow|^2 \sin \phi} \left(|\downarrow\rangle - e^{i\delta} |\uparrow\rangle \right) |\alpha_\downarrow(e^{i\phi} - 1)\rangle + \\ & + e^{i|\alpha_\uparrow|^2 \sin \phi} \left(|\downarrow\rangle + e^{i\delta} |\uparrow\rangle \right) |\alpha_\uparrow(e^{i\phi} - 1)\rangle \Big]. \end{aligned} \quad (41)$$

In a single run of the experiment the probability to find the ion in the $|\downarrow\rangle$ state is

$$P_{\downarrow}(\phi) = |\langle\downarrow|\psi\rangle|^2 = \frac{1}{2} \left\{ 1 - \exp \left[-|\Delta\alpha|^2(1 - \cos\phi) \right] \times \right. \\ \left. \times \cos \left[\delta + (|\alpha_{\downarrow}|^2 - |\alpha_{\uparrow}|^2) \sin\phi + 2(1 - \cos\phi) \text{Im} \alpha_{\downarrow}^* \alpha_{\uparrow} \right] \right\}. \quad (42)$$

The phase shift ϕ is taken to be a Gaussian distributed random variable with standard deviation σ . The average of $P_{\downarrow}(\phi)$ is

$$P_{\downarrow} = \frac{1}{2} \left\{ 1 - \frac{1}{\sqrt{2\pi\sigma^2}} \int_{-\infty}^{\infty} \exp \left(-\frac{\phi^2}{2\sigma^2} - |\Delta\alpha|^2(1 - \cos\phi) \right) \times \right. \\ \left. \times \cos \left[(|\alpha_{\downarrow}|^2 - |\alpha_{\uparrow}|^2) \sin\phi \right] \cos \left[\delta + 2(1 - \cos\phi) \text{Im} \alpha_{\downarrow}^* \alpha_{\uparrow} \right] d\phi \right\}, \quad (43)$$

where the odd part of the integrand vanishes. We note that in general there is a phase shift to the fringes even though the distribution of ϕ is symmetric. In general this integral does not simplify. However, in the case of experimental interest, $\alpha_{\downarrow} \propto \alpha_{\uparrow}$ (specifically, $\alpha_{\downarrow} = -2\alpha_{\uparrow}$) in which case $\text{Im} \alpha_{\downarrow}^* \alpha_{\uparrow} = 0$. We further make the small angle approximation in the integrand, which is valid if $\sigma^2 \ll 1$, when the term $e^{-\phi^2/2\sigma^2}$ dominates; or, if $|\Delta\alpha| \gg 1$ and $\sigma \leq \pi$, when the term $e^{-|\Delta\alpha|^2(1-\cos\phi)}$ dominates. In these regimes, the integral can be evaluated analytically to yield the signal

$$P_{\downarrow} = \frac{1}{2} \left\{ 1 - \frac{\cos\delta}{\sqrt{1 + |\Delta\alpha|^2\sigma^2}} \exp \left[\frac{-(|\alpha_{\downarrow}|^2 - |\alpha_{\uparrow}|^2)^2\sigma^2}{2(1 + |\Delta\alpha|^2\sigma^2)} \right] \right\}. \quad (44)$$

This approximate expression provides a good guide to the behavior and can be used for a simplified comparison to the data. We note that in the experimentally accessible regime of $|\Delta\alpha| \sim 1$ –4 and $\sigma \leq 2$, Equation 44 is accurate to about 10% even though the small angle approximation is not strictly valid.

b. Fock state interferometer and phase reservoir We start in the state $[|n\rangle + |m\rangle]|\downarrow\rangle/\sqrt{2}$. We again denote the ion oscillation phase shift by ϕ , and the phase shifted superposition is

$$|\psi\rangle = \frac{1}{\sqrt{2}} |\downarrow\rangle (e^{-im\phi}|m\rangle + e^{-in\phi}|n\rangle). \quad (45)$$

In the second beam splitter a $-\pi$ pulse again entangles the spins with the motion, as

$$|\psi\rangle = \frac{1}{\sqrt{2}} (e^{-im\phi}|\downarrow\rangle|0\rangle + e^{-in\phi}|\uparrow\rangle|n'\rangle). \quad (46)$$

A final $\pi/2$ pulse generates the state

$$|\psi\rangle = \frac{1}{2} \left[(e^{-im\phi} - e^{i(\delta-n\phi)})|\downarrow\rangle|0\rangle + (e^{-in\phi} + e^{i(\delta-m\phi)})|\uparrow\rangle|n'\rangle \right]. \quad (47)$$

The projection onto $|\downarrow\rangle$ yields

$$P_{\downarrow}(\phi) = |\langle \downarrow | \psi \rangle|^2 = \frac{1}{2} \left[1 + \cos(\delta + (n - m)\phi) \right]. \quad (48)$$

Again, the phase shift introduced between the beamsplitter pulses results in a shift of the fringes. The random phase shifts ϕ are assumed to be Gaussian distributed with standard deviation σ , and the ensemble average of $P_{\downarrow}(\phi)$ is

$$P_{\downarrow} = \frac{1}{2} \left[1 + e^{-(n-m)^2 \sigma^2 / 2} \cos \delta \right]. \quad (49)$$

The decoherence scales exponentially with the square of the difference in the Fock state indices, $n - m$, so that “larger” superpositions lose coherence exponentially faster. Compare the scaling of the decay of the fringe contrast as a function of $n - m$ in Eq. 49 with the decay of the off-diagonal elements of the density matrix ρ_{mn} given in Equation 21. The results are equivalent.

C. Connection of averaged interferometer approach and master equation

It is reasonable to ask in what sense the interferometer experiments of Section II B directly probe the relevant off-diagonal matrix elements as calculated in Section II A. In the case of Fock states interacting with the phase reservoir (Sections II A 2 a and II B 3 b), the connection is quite simple, in other cases, the connection is not as straightforward.

1. Spin coherence

In this section we argue that the contrast of the interference fringes is a measure of the coherence of the combined spin and motional quantum state, and that the spin part can be negligible or can be removed. To address this issue, we consider the interferometer experiment in the case of no added noise. We take the example of the cat state interferometer discussed in Section II B and write the cat state of the system after the first $\pi/2$ and displacement pulses (assumed to be short) as a density matrix (the wavefunction for $\mathcal{C} = 1$ is given in Equation 25):

$$\rho = \frac{1}{2} [|\alpha_{\downarrow}\rangle | \downarrow \rangle \langle \downarrow | \langle \alpha_{\downarrow} | + |\alpha_{\uparrow}\rangle | \uparrow \rangle \langle \uparrow | \langle \alpha_{\uparrow} + \mathcal{C} | \alpha_{\downarrow} | | \downarrow \rangle \langle \uparrow | \langle \alpha_{\uparrow} + \mathcal{C}^* | \alpha_{\uparrow} | | \uparrow \rangle \langle \downarrow | \langle \alpha_{\downarrow} |], \quad (50)$$

where $\mathcal{C} = \mathcal{C}_s \mathcal{C}_m$ quantifies the coherence which has contributions from both the spin (\mathcal{C}_s) and motion (\mathcal{C}_m). This separation of the contrast into a product of spin and motion contributions is valid for reservoirs in which the spin and motion are not coupled, such as the amplitude, natural and phase reservoirs. The only reservoir experiments in which the spin decoherence is not negligible are the natural reservoir experiments, since for all of our applied reservoirs the time of application is short. For the natural reservoir experiments, we are forced to simply wait a time t for the ambient noise to act on the system. To within experimental errors, we can adequately characterize spin decoherence as exponential, $C_s = \exp(-\gamma_s t)$. Note that the separation of coherences is valid if the spin undergoes only phase decay, with no random spin-flip transitions, which is verified in our experiments.

We now consider, for simplicity, the case in which there is no interaction with the reservoir, and the second displacement is applied, undoing the first displacement, leaving

$$\rho = \frac{1}{2} [|0\rangle | \downarrow \rangle \langle \downarrow | \langle 0| + |0\rangle | \uparrow \rangle \langle \uparrow | \langle 0| + \mathcal{C}|0\rangle | \downarrow \rangle \langle \uparrow | \langle 0| + \mathcal{C}^*|0\rangle | \uparrow \rangle \langle \downarrow | \langle 0|]. \quad (51)$$

The final $\pi/2$ -pulse with phase δ transforms the spins as in Eqs. 30, and the detection of $| \downarrow \rangle$ with trace over the motion leaves:

$$P_{\downarrow} = \frac{1 - \text{Re}(\mathcal{C}) \cos \delta}{2}. \quad (52)$$

Thus the contrast of the Ramsey fringes depends directly on the coherence. Separate experiments verify that the spin is not disturbed by or during the time of application of our engineered phase, amplitude and zero-temperature reservoirs, so that in these experiments the fringe contrast is a simple probe of the change in motional coherence.

2. Cats, amplitude noise

The interferometer calculations presented in Section II B predict the outcome of particular experiments. The master equation solutions in Section II A do not. In this section, we take the solution of the master equation, in terms of the time-evolution of a density matrix and derive a prediction for an interferometer experiment. The result is shown to be equivalent to the average-over-classical-variables approach in Section II B. We do this for the Schrödinger Cat interferometer subject to amplitude noise. The solution to the master equation was given in Section II A 1. It is a straightforward matter to add the spin part to this solution, which must be done for the interferometer calculation. Starting from Eq. 14, we divide the initial density matrix (written as an initial P -function $P_0(\mu, \nu^*)$) into four parts, corresponding to the initial state $|\psi\rangle = (| \downarrow \rangle | \alpha_{\downarrow} \rangle + | \uparrow \rangle | \alpha_{\uparrow} \rangle) / \sqrt{2}$:

$$P_0(\mu, \nu^*) = P_0^{(1)}(\mu, \nu^*) + P_0^{(2)}(\mu, \nu^*) + P_0^{(3)}(\mu, \nu^*) + P_0^{(4)}(\mu, \nu^*) \quad (53)$$

with

$$P_0^{(1)}(\mu, \nu^*) = \frac{1}{2} \delta(\mu - \alpha_{\downarrow}) \delta(\nu - \alpha_{\downarrow}) | \downarrow \rangle \langle \downarrow | \quad (54)$$

$$P_0^{(2)}(\mu, \nu^*) = \frac{1}{2} \delta(\mu - \alpha_{\uparrow}) \delta(\nu - \alpha_{\uparrow}) | \uparrow \rangle \langle \uparrow | \quad (55)$$

$$P_0^{(3)}(\mu, \nu^*) = \frac{1}{2} \langle \alpha_{\uparrow} | \alpha_{\downarrow} \rangle \delta(\mu - \alpha_{\downarrow}) \delta(\nu - \alpha_{\uparrow}) | \downarrow \rangle \langle \uparrow | \quad (56)$$

$$P_0^{(4)}(\mu, \nu^*) = [P_0^{(3)}(\mu, \nu^*)]^{\dagger}. \quad (57)$$

From Eq. 14 this leads to four contributions to $\rho(t)$

$$\rho(t) = \rho^{(1)}(t) + \rho^{(2)}(t) + \rho^{(3)}(t) + \rho^{(4)}(t) \quad (58)$$

with

$$\rho^{(1)}(t) = \frac{1}{2} \mathcal{D}(\bar{\alpha}_{\downarrow}) \rho_T(t) \mathcal{D}^{\dagger}(\bar{\alpha}_{\downarrow}) |\downarrow\rangle\langle\downarrow| \quad (59)$$

$$\rho^{(2)}(t) = \frac{1}{2} \mathcal{D}(\bar{\alpha}_{\uparrow}) \rho_T(t) \mathcal{D}^{\dagger}(\bar{\alpha}_{\uparrow}) |\uparrow\rangle\langle\uparrow| \quad (60)$$

$$\rho^{(3)}(t) = \frac{1}{2} \langle\alpha_{\uparrow}|\alpha_{\downarrow}\rangle^{1-\frac{e^{-\gamma t}}{1+2N(t)}} \mathcal{D}(\bar{\alpha}_{\downarrow}) \rho_T(t) \mathcal{D}^{\dagger}(\bar{\alpha}_{\uparrow}) |\downarrow\rangle\langle\uparrow| \quad (61)$$

$$\rho^{(4)}(t) = (\rho^{(3)}(t))^{\dagger} \quad (62)$$

where $\bar{\alpha}_{\downarrow,\uparrow}$ are defined as in Eqs. 15,16. To complete the experiment, we apply a second displacement, which is given by the operator

$$|\downarrow\rangle\langle\downarrow| \mathcal{D}(\alpha_{\downarrow} e^{-i\theta}) + |\uparrow\rangle\langle\uparrow| \mathcal{D}(\alpha_{\uparrow} e^{-i\theta}), \quad (63)$$

where θ is the phase of the second displacement with respect to that of the first. We then apply the final $\pi/2$ Ramsey pulse which transforms the spins as in Eq. 30 and measure the probability that the ion is in the spin-down state, as discussed in the context of Eq. 23. Thus we are interested only in the component of ρ given by $\rho_{\downarrow} \equiv \langle\downarrow|\rho_f|\downarrow\rangle$ where ρ_f is the density matrix after the final displacement and Ramsey pulses. Furthermore, since we do not measure the motional state, a trace over the motional degrees of freedom is required:

$$P_{\downarrow}(t) = \text{Tr}_n \rho_{\downarrow}(t) = \sum_n \langle n | \rho_{\downarrow}(t) | n \rangle. \quad (64)$$

The quantity ρ_{\downarrow} is given by:

$$\rho_{\downarrow}(t) = \rho_{\downarrow}^{(1)}(t) + \rho_{\downarrow}^{(2)}(t) + \rho_{\downarrow}^{(3)}(t) + \rho_{\downarrow}^{(4)}(t) \quad (65)$$

with

$$\rho_{\downarrow}^{(1)}(t) = \frac{1}{4} \mathcal{D}(\alpha_{\downarrow} e^{-i\theta}) \mathcal{D}(\bar{\alpha}_{\downarrow}) \rho_T(t) \mathcal{D}^{\dagger}(\bar{\alpha}_{\downarrow}) \mathcal{D}^{\dagger}(\alpha_{\downarrow} e^{-i\theta}) \quad (66)$$

$$\rho_{\downarrow}^{(2)}(t) = \frac{1}{4} \mathcal{D}(\alpha_{\uparrow} e^{-i\theta}) \mathcal{D}(\bar{\alpha}_{\uparrow}) \rho_T(t) \mathcal{D}^{\dagger}(\bar{\alpha}_{\uparrow}) \mathcal{D}^{\dagger}(\alpha_{\uparrow} e^{-i\theta}) \quad (67)$$

$$\rho_{\downarrow}^{(3)}(t) = -\frac{1}{4} e^{i\delta} \langle\alpha_{\uparrow}|\alpha_{\downarrow}\rangle^{1-\frac{e^{-\gamma t}}{1+2N(t)}} \mathcal{D}(\alpha_{\downarrow} e^{-i\theta}) \mathcal{D}(\bar{\alpha}_{\downarrow}) \rho_T(t) \mathcal{D}^{\dagger}(\bar{\alpha}_{\uparrow}) \mathcal{D}^{\dagger}(\alpha_{\uparrow} e^{-i\theta}) \quad (68)$$

$$\rho_{\downarrow}^{(4)}(t) = (\rho_{\downarrow}^{(3)}(t))^{\dagger}. \quad (69)$$

In what follows, we assume that $\alpha_{\downarrow,\uparrow}$ are real. Performing the trace, we find that $\text{Tr}_n \rho_{\downarrow}^{(1)} = \text{Tr}_n \rho_{\downarrow}^{(2)} = 1/4$ and that $\text{Tr}_n \rho_{\downarrow}^{(3,4)}$ give rise to the interference. Using the identity

$$\mathcal{D}(\kappa) \mathcal{D}(\lambda) = e^{\frac{1}{2}(\kappa\lambda^* - \kappa^*\lambda)} \mathcal{D}(\kappa + \lambda), \quad (70)$$

substituting for ρ_T from Eq. 17 and using the closure relation $\sum_m |m\rangle\langle m| = 1$,

$$\text{Tr}_n \rho_{\downarrow}^{(3)}(t) = \frac{1}{1+N(t)} e^{i(\alpha_{\uparrow} - \alpha_{\downarrow})(\bar{\alpha}_{\downarrow} + \bar{\alpha}_{\uparrow}) \sin \theta} \sum_m \left(\frac{N(t)}{1+N(t)} \right)^m \mathcal{L}_m(|\beta|^2) e^{-\frac{1}{2}|\beta|^2} \quad (71)$$

where $\beta = \alpha_{\uparrow} e^{-i\theta} + \bar{\alpha}_{\uparrow} - \alpha_{\downarrow} e^{-i\theta} + \bar{\alpha}_{\downarrow}$ and \mathcal{L} is a Laguerre polynomial which comes from $\langle m | \mathcal{D}(\kappa) | m \rangle = \exp(-|\kappa|^2/2) \mathcal{L}_m(|\kappa|^2)$. Using $\sum_m \epsilon^m \mathcal{L}_m(x) = \exp[-\epsilon x/(1-\epsilon)]$ and further simplifying,

$$P_{\downarrow}(t) = \frac{1}{2} - \frac{1}{2} e^{-(\alpha_{\downarrow} - \alpha_{\uparrow})^2 [1 + \bar{n}(1 - e^{-\gamma t}) + e^{-\gamma t/2} \cos \theta]} \cos \left[\delta + e^{-\gamma t/2} (\alpha_{\uparrow}^2 - \alpha_{\downarrow}^2) \sin \theta \right]. \quad (72)$$

For all of our experiments we can consider the high-temperature, short-time limits: $\bar{n} \gg 1$ and $\gamma t \ll 1$. In this limit,

$$P_{\downarrow}(t) = \frac{1}{2} \left\{ 1 - e^{-(\alpha_{\downarrow} - \alpha_{\uparrow})^2 [1 + \bar{n}\gamma t + \cos \theta]} \cos \left[\delta + (1 - \gamma t/2) (\alpha_{\uparrow}^2 - \alpha_{\downarrow}^2) \sin \theta \right] \right\}. \quad (73)$$

Normally, the second displacement is the reverse of the first ($\theta = \pi$) and the Ramsey fringes in Eq. 33 are recovered with the association $\bar{n}\gamma t \rightarrow 2\sigma^2$. The scaling with the square of the size of the initial state is evident. The constant term in the exponential measures a residual overlap between the initial state and the final state, present even in the infinite time limit.

Similar procedures to this for other types of initial states and reservoirs yield results that agree with those from the interferometer averaging over random displacements/phases approach given in Section II B.

III. EXPERIMENT

A. Ion Trap

We use a miniaturized version of the linear Paul trap [21]. A diagram of the trap structure is shown in Fig. 4. It consists of two alumina wafers separated by 200 μm with alumina spacers (not shown). Each wafer has a slot 2 mm long by 200 μm wide. Gold is deposited onto the edges of the slot to form electrodes. One side of the slot is the rf electrode, and the other side is divided into three segments to which different static potentials are applied to make a static well along the z -axis. The segmented electrodes are formed by cutting two side slots of width 20 μm . The side slots are separated by 200 μm , forming two “endcaps” and one “middle” electrode. When the wafers are sandwiched together with the spacers, the four interior edges of the main slots approximate the four wires of a linear quadrupole trap. The microfabricated structure described here allows miniaturization of the linear trap and correspondingly high trap strength.

The linear trap is mounted at the end of an rf quarter-wave coaxial resonator that supplies the required rf voltage [22]. The trap and coaxial resonator are contained within an UHV enclosure, as in Ref [22]. The two rf electrodes are connected to the tip of the coaxial center conductor. Each of the static-potential segments are connected to UHV feedthroughs through a pair of 200 kHz RC low-pass filters in series. The coaxial resonator is 30 cm long, partially filled with alumina to lower its resonance frequency to $\Omega_T/2\pi = 113$ MHz. With 8 W of rf power, the radial secular frequencies are approximately 13 MHz. The axial potential is controlled by the static potentials applied to the segmented electrodes. Positive potentials are applied to the endcaps to confine positive ions in the middle of the trap. For the data presented in this paper, we restrict our attention to the axial mode of motion. With 30 V applied to the endcap segments and the middle segments and rf electrodes held at static ground potential, the axial frequency is $\omega_z/2\pi = 11.3$ MHz.

B. Raman transitions and cooling the ion

The level structure of ${}^9\text{Be}^+$ is shown in Fig. 5. We select two states from the ground state hyperfine manifold: the $|F = 2, m_F = -2\rangle$ state, which we label $|\downarrow\rangle$, and the $|F = 1, m_F = -1\rangle$ state, which we label $|\uparrow\rangle$. The ion is Doppler cooled by applying circularly polarized light detuned ~ 8 MHz below the strongly-allowed ($\Gamma/2\pi = 19$ MHz) cycling transition $2s\,{}^2S_{1/2}|2, -2\rangle \rightarrow 2p\,{}^2P_{3/2}|3, -3\rangle$ (beam D2 of Fig. 5). Due to imperfect σ^- polarization the ion optically pumps to the $|1, -1\rangle$ state with a probability $\sim 1 \times 10^{-4}$. To prevent a loss of cooling from these decay events, we apply laser light resonant with the transition $2s\,{}^2S_{1/2}|1, -1\rangle \rightarrow 2p\,{}^2P_{1/2}|2, -2\rangle$. This transition is labeled D1 in Fig. 5. After Doppler cooling, the mean occupation number of the axial mode of motion is $\langle n \rangle \approx 1$.

We efficiently detect (See Fig. 6) the $|\downarrow\rangle$ internal state of the ion by applying Doppler beam D2 with no D1 light [18]. The fluorescence collection system has a $f/1.2$ aperture, and the light is transferred onto the photocathode of a photomultiplier tube. The PMT quantum efficiency is $\approx 30\%$. After all losses at windows and filters, the overall scattered-photon detection efficiency is measured to be $\approx 1.5 \times 10^{-3}$. For detection, the laser is at the same detuning as for Doppler cooling and the intensity is kept well below saturation $I \sim 0.1I_{\text{sat}}$. During a $200\,\mu\text{s}$ detection period, we collect an average of 10 photons if the ion is in the $|\downarrow\rangle$ state, and 0.1 photons if it is in the $|\uparrow\rangle$ state. The photon distributions are Poissonian. By averaging the number of photons detected in successive repetitions of a given experiment and normalizing to the count rate when the ion is prepared in a control experiment in the $|\downarrow\rangle$ state (by simple optical pumping), we determine the probability P_{\downarrow} .

In previous experiments using miniature spherical quadrupole ion traps (see e.g., Ref. [24]), ion internal state discrimination was limited by sidebands on the $2s\,{}^2S_{1/2}\,F = 1 \rightarrow 2p\,{}^2P_{1/2}, F = 2$ transition due to ion micromotion at frequency Ω_T . Thus a laser tuned to transition D2 would weakly drive an ion in the $|\uparrow\rangle$ state. The miniature linear trap addresses the issue of micromotion in two ways. First, there is negligible micromotion associated with the confinement along the axis of the trap. Second, the close proximity of the static potential electrodes permits accurate cancellation of stray static fields, resulting in negligible sidebands on the transitions from micromotion. This permits state discrimination of 97% in a single experiment. This is shown in Figure 6. Even in the absence of micromotion, detection efficiency is limited by off-resonant optical pumping of the $|\uparrow\rangle$ state by the detection laser [23].

We drive coherent stimulated Raman transitions with a pair of laser beams (such as R1 and R2 shown in Figure 5) detuned $\Delta/2\pi \approx 10$ to 20 GHz from the $2s\,{}^2S_{1/2} \rightarrow 2p\,{}^2P_{1/2}$ transition near $\lambda = 313$ nm. The Raman beams are derived from a single dye laser beam that is frequency doubled, and the difference frequency between the two Raman beams is generated with several acousto-optic modulators in series. We employ three types of Raman transitions, distinguished by beam geometry and difference frequency [16,25]. The beam geometry sets the projection of photon momentum onto the axis of the trap (\hat{z}), characterized by the wavevector difference $\delta\mathbf{k} = (\mathbf{k}_1 - \mathbf{k}_2) \cdot \hat{z}$. The coupling of this photon momentum to the motion of the ion is parametrized by the Lamb-Dicke parameter, $\eta = \delta k z_0$, where $z_0 = \sqrt{\hbar/2m\omega} \approx 7$ nm is the harmonic oscillator characteristic length for axial motion.

The three types of Raman transitions are as follows. (i) Copropagating beams ($\delta k \approx 0$) drive a motion-independent “spin-flip” transition, $|\uparrow\rangle|n\rangle \leftrightarrow |\downarrow\rangle|n\rangle$. The frequency difference

between the Raman beams is set equal to the frequency difference between the states, $\omega_0 = \omega_{hf} + \omega_Z$, where $\omega_{hf}/2\pi \approx 1.25$ GHz is the hyperfine splitting and $\omega_Z/2\pi \approx 12$ MHz is the Zeeman splitting due to an applied magnetic field $|\mathbf{B}| \approx 0.57$ mT. (ii) Beams oriented 45° to the trap axis and 90° to each other result in a wavevector difference pointing along the trap axis with $\delta k = 2\sqrt{2}\pi/\lambda$ and couple to the axial motion. For the conditions of this experiment, $\eta \approx 0.20$. These beams at difference frequencies $\omega_0 + \omega\Delta n$, couple the states $|\downarrow\rangle|n\rangle$ and $|\uparrow\rangle|n + \Delta n\rangle$. In the Lamb-Dicke limit, $(\eta^2\langle n \rangle \ll 1)$, the strength of the sideband coupling is proportional to $\eta^{|\Delta n|}$. The Raman beams in cases (i) and (ii) are linearly polarized, with one beam polarized parallel to the quantization axis ($\Delta m = 0$) and the other polarized perpendicular ($\Delta m = \pm 1$). Note that only the σ^- component of the latter beam is required to drive the Raman transition, but the use of linear polarized light reduces the Stark shifts relative to the case of using circularly polarized light. (iii) Beams oriented as in (ii), with difference frequency set equal to the axial secular motion frequency ω approximate the harmonic oscillator displacement operator $\mathcal{D}(\alpha)$, defined by the relation $\mathcal{D}(\alpha)|0\rangle = |\alpha\rangle$, and $|\alpha\rangle$ is a coherent state. In the Lamb-Dicke limit, the displacement $|\alpha| = \eta\Omega_{\mathcal{D}}t$ is proportional to the duration of the laser pulse t and the Rabi frequency $\Omega_{\mathcal{D}}$, and θ is set by the phase and polarization of the applied laser fields. In this case, the two Raman beams are linearly polarized such that the polarization vectors are mutually orthogonal to both each other and to the quantization axis. This cancels Stark shifts to a high degree and results in the two spin states being simultaneously displaced in opposite directions such that $\alpha_{\uparrow} = -\alpha_{\downarrow}/2$.

The ion is first prepared in the ground state of motion with resolved sideband Raman cooling [18]. Raman cooling consists of repeatedly driving the first red-Raman sideband of the axial-motion-sensitive transition, case (ii) with $\Delta n = -1$, followed by optical pumping to the $|\downarrow\rangle$ state after each Raman pulse. The optical pumping is achieved with D1 and D3 ($2s^22S_{1/2}|2, -1\rangle \rightarrow 2p^22P_{1/2}|3, -2\rangle$, see Fig. 5) applied. The rate at which the ion undergoes the red sideband Raman transition depends on the initial state of motion as $\Omega_{\text{rsb}} \propto \sqrt{n}$. The duration of the successive Raman pulses is progressively lengthened, so as to successively drive π pulses on the $n_i \rightarrow n_i - 1, n_i - 1 \rightarrow n_i - 2$, etc., transitions, where n_i is the total number of cooling pulses. The final pulse of this sequence is selected to drive a π pulse on the $|\downarrow\rangle|1\rangle \rightarrow |\uparrow\rangle|0\rangle$ transition. After each Raman pulse, we drive the D1 and D3 transitions for $5\mu\text{s}$, optically pumping any population in the $|\uparrow\rangle$ state, or the (2,-1) state to the $|\downarrow\rangle$ state. Typically, after 6 cycles of Raman cooling, the ion has a probability of 95% to be in the ground state $|\downarrow\rangle|0\rangle$.

C. Ion interferometry: techniques

In the experiments reported here, we measure the coherence of quantum superpositions with single-atom interferometry, analogous to that used in our previous work [10] and discussed in Section II B. The motional state of the ion is split into a superposition of two parts. The “beamsplitters” of our interferometers consist of a pair of stimulated Raman pulses. We employ two types of interferometers, both discussed in Section II B.

1. Ion interferometry: Cat states

The Schrödinger cat interferometer starts with the usual ground state ($|\downarrow\rangle|0\rangle$) preparation. The first pulse is then a $\pi/2$ pulse on the motion-independent transition (i), with drive time typically $T_{\pi/2} \approx 0.3 \mu\text{s}$ which generates an equal spin superposition, $|\downarrow\rangle|0\rangle \rightarrow (|\downarrow\rangle + |\uparrow\rangle)|0\rangle/\sqrt{2}$ as indicated schematically in Figure 1, panel (1).

We drive Raman transition (iii) to excite the motion associated with each spin state into a coherent state, resulting in the state of Eq. 25. We call this the displacement pulse [Figure 1, panel (2)]. We vary the length of the Raman drive pulse in order to vary $|\alpha_\downarrow|$ and $|\alpha_\uparrow|$. We independently measure $|\alpha_\downarrow|$ and $|\alpha_\uparrow|$ in the following manner [17] (which is also discussed in the context of Equations 85 and 86, below). The ion is prepared in a coherent state, and then Raman transition (ii), tuned to the first blue sideband, is driven for a variable time t_p . After this “probe” Raman transition, we determine the probability $P_\downarrow(t_p)$. The resulting curve may be decomposed into sums of sinusoids that correspond to $\Delta n = 1$ transitions between Fock states. The Fock state distribution is then fit to that of a coherent state, thereby extracting $|\alpha|$ [17]. The values of $|\alpha_\downarrow|$ and $|\alpha_\uparrow|$ are measured separately, by preparing the ion in either the $|\downarrow\rangle|0\rangle$ state or in the $|\uparrow\rangle|0\rangle$ state, applying the coherent drive pulse, and then probing and detecting as just described. Curves of $|\alpha_{\downarrow,\uparrow}|$ vs. the length t of the displacement pulse are shown in Fig. 7(b). The ratio $|\alpha_\downarrow|/|\alpha_\uparrow| = 2.0 \pm 0.1$, averaged over the data set, is consistent with the expected value of 2. The slope $d|\Delta\alpha|/dt = \eta\Omega$ is consistent with the expected value.

The Schrödinger cat interferometer is completed by applying a second coherent displacement pulse 180° out of phase from the first displacement pulse [Figure 1, panel (4)]. The phase of the displacement is set by the phase of an oscillator that drives an AO that is in one of the Raman beams. All phases are referenced to a master oscillator by phase locking to that oscillator. If the motion was unperturbed during the time between the displacement pulses, then the inverse displacement would restore the motion associated with each spin state to the ground state of motion. The wave function would return to $|\psi\rangle = (|\downarrow\rangle + |\uparrow\rangle)|0\rangle/\sqrt{2}$. A second $\pi/2$ pulse on the motion-independent spin-flip transition, with phase δ relative to the first $\pi/2$ pulse, interferes the spin components. The probability $P_\downarrow(\delta)$ varies sinusoidally with δ . To record $P_\downarrow(\delta)$, we step the frequency of the oscillator controlling the $\pi/2$ pulses and bin the fluorescence counts at each step. Here, δ is the accumulated phase difference caused by the frequency difference between the oscillator frequency ν and ν_0 as in normal Ramsey spectroscopy. We typically repeat the experiment 100 times at each step. Note that the resulting fringe spacing is much smaller than the width of the Rabi pedestal, meaning that the predominant effect is a change in phase, without introducing significant inaccuracy in the $\pi/2$ pulse. We typically record three oscillations of P_\downarrow . The fringes are fit with a sinusoid $A + B \cos(\omega - \omega_0)T$, where T is the time between spin pulses. The contrast of the fringes is defined as B/A . For the basic interferometer just described, with no perturbations of the motion between the “beam splitter” pulses, the contrast is typically 0.6–0.8. This contrast differs from unity for several reasons. (1) Errors in the $\pi/2$ spin flip pulses, primarily due to laser power fluctuations. (2) Fluctuating magnetic fields which reduce the spin coherence through fluctuating Zeeman shifts. (3) motional heating during and between the displacement pulses, with further small contributions due to inaccuracies in reversing the initial displacement pulse. These effects are expected to be random and should not influence

the additional decoherence caused by the applied reservoir (see Section II C).

2. Interferometry: Fock state interferometer

The Fock state interferometer beamsplitters combine a $\pi/2$ -pulse with a π -pulse on transitions of either type (i) or (ii), as shown in Table 1. As an example, consider the generation of the superposition $|\downarrow\rangle(|0\rangle + |2\rangle)/\sqrt{2}$. A $\pi/2$ -pulse on the first blue sideband, transition type (ii) with $\Delta n = +1$ and duration $T_{\pi/2} \approx 1 \mu\text{s}$, drives the transition $|\downarrow\rangle|0\rangle \rightarrow (|\downarrow\rangle|0\rangle + |\uparrow\rangle|1\rangle)/\sqrt{2}$. A π pulse on the first red sideband, transition type (ii) with $\Delta n = -1$ and duration $T_{\pi} \approx 1.5 \mu\text{s}$, drives the transition $|\uparrow\rangle|1\rangle \rightarrow |\downarrow\rangle|2\rangle$. This second pulse does not affect the population in the $|\downarrow\rangle|0\rangle$ state. The result of these two pulses is the desired state $|\psi\rangle = |\downarrow\rangle(|0\rangle + |2\rangle)/\sqrt{2}$. The second beamsplitter recombines the two parts of the wavefunction by driving a second π -pulse on the red sideband followed by a $\pi/2$ -pulse on the blue sideband. By sweeping the frequency of the blue sideband oscillator we generate Ramsey fringes in the probability P_{\downarrow} . Contrast (without coupling to the reservoir) is limited by the same mechanisms as in the Schrödinger-cat interferometer.

D. Engineering reservoirs: techniques

1. High-temperature amplitude reservoir

As discussed in the introduction, the motion of a trapped ion couples to environmental electric fields \mathbf{E} through the potential $U = -q\mathbf{x} \cdot \mathbf{E}$, where \mathbf{x} is the position of the ion relative to its equilibrium position (proportional to the amplitude of motion) and q is the charge of the ion. If \mathbf{E} is due to a reservoir of fluctuating field modes, then $\mathbf{E} \propto \sum_i \epsilon_i (\hat{b}_i + \hat{b}_i^\dagger)$ where \hat{b}_i , \hat{b}_i^\dagger are the lowering and raising operators of the field modes (as in Section II A 1). A classical coherent drive (for which \mathbf{E} is a narrow-band sine-wave) applied to the trap electrodes at the ion axial motional frequency ω results in a displacement of the motional state proportional to the size and duration of the applied field. This is shown in Figure 7(a) for two different durations of the applied field. We simulate the effects of the high-temperature amplitude reservoir discussed in Section II A 1 by applying *random* electric fields along the axis of the trap, whose spectrum is centered on the ion axial motion frequency ω .

To generate the required axial fields, we apply a potential to one of the endcap electrodes. This generates both an axial field and a small radial field. We ignore the effect of the radial field since we are insensitive to motion in the radial direction. This field also modulates the axial potential and gives rise to an accompanying (random) phase shift; however, for the experimental conditions this phase shift is negligible. We start with a 10 MHz bandwidth noise source that rolls off at 6 dB/octave starting at 10 MHz. We filter the noise such that the resulting noise spectrum has 3 dB points at 9 MHz and 11.5 MHz, and the noise rolls off at 6 dB/octave above and below these points. This spectral noise is applied to the trap electrodes through a network of RC lowpass filters designed to prevent such fields from reaching the static trap electrodes. The filters effectively limit ambient noise from reaching the electrodes, but large deliberately applied fields can still be effective. The noise is applied for $3 \mu\text{s}$ between the Ramsey zones. The total time for the Ramsey experiment (the time

between the $\pi/2$ spin-pulses) is about $T = 20 \mu\text{s}$ and is held fixed. For these filters, trap geometry and application time it can be shown that this type of drive correctly simulates an infinite-bandwidth, amplitude-only reservoir.

2. Phase reservoir

A phase reservoir as described in Section II A 2 is simulated by random variations in the trap frequency ω , changing the phase of the ion oscillation without changing its energy. We realize this coupling experimentally by adiabatically modulating the trap frequency. The random potential fluctuations are filtered through a low-pass network with a cut-off frequency well below ω to maintain adiabaticity and to avoid any power at the trap secular frequency, which may cause amplitude noise. The potential fluctuations are applied to one of the middle electrodes, which is symmetric with respect to the axial direction, so as to produce field gradients and minimize any applied uniform axial fields further reducing the possibility of changing the motional energy. Applying a potential to just one middle electrode does result in a radial field, but as before, we isolate the axial motion and ignore any radial motion.

In the phase reservoir, the ion follows the change in trap frequency in the sense that there is no change in the energy of the trap motion, however the phase is either advanced or retarded relative to the unperturbed motion. We start with a 10 MHz pseudo-random noise source and filter the noise, creating a spectrum that is flat between 1 kHz and 100 kHz with a roll-off of 12 dB/octave above 100 kHz and 6 dB/octave below 1 kHz. The phase deviation of the ion motion is related to the voltage deviation on the electrodes. The trap axial frequency is related to the voltage difference between the endcap and middle segments by the relation $\omega \propto \sqrt{V_0}$. The deviation of the trap frequency is given by $\delta\omega/\omega \approx \delta V/4V_0$ since only one electrode is driven. The phase shift of the ion motion is the integral of the frequency deviation over the time of the noise pulse T_n , $\delta\phi \equiv \int_0^{T_n} \delta\omega_z dt = \int_0^{T_n} \omega_z (\delta V/2V_0) dt$. Typically $T_n = 10 \mu\text{s}$. We cannot directly measure the voltage on the trap electrodes since some of the filters between our noise generator and the electrodes are within the vacuum enclosure. However, on a mock-up of the trap electrodes and the associated filters, we measured the voltage deviations with an integrating circuit. These measurements verified that the phase deviations are Gaussian distributed, with a width that varies with the applied noise voltage, and that negligible voltage noise is added at the trap secular frequency. In separate experiments, we verified that the change in motional energy was negligible during the application of the phase reservoir.

3. Natural reservoir

The third type of reservoir is not engineered, but is the ambient, or “natural” noise in our trap. We have previously observed heating in miniaturized Paul traps [26]. We have further determined that this ambient noise is dominated by uniform field fluctuations rather than field-gradient fluctuations [27]. We do not currently have an explanation of the heating mechanism. However, thermal or Johnson noise, background gas collisions, and several other sources are too small to explain the heating rate. We do know that this ambient noise

source adds energy to the ion (amplitude noise), and that the state of the ion evolves into a thermal state with steadily increasing temperature. The suspected cause is fluctuating patch-potentials at the trap electrodes, a problem that is exacerbated by the small size of our trap [26]. To observe the effects of this heating on quantum coherences, we simply run the Ramsey interferometer experiment with varying time between the Ramsey pulses.

We can also observe the effect of the heating on the energy of the motional state. We find that due to our unknown environmental source of noisy electric fields, the ion heats from the ground state at a rate linear in time with $\partial\langle n\rangle/\partial t \sim 5.7 \pm 1$ quanta per ms. Shown in Figure 8 are data for the mean quantum number in the motion as a function of delay time. That is, the ground state is prepared and the average quantum number is measured after a fixed delay time t . At each point the motional state is thermal as determined by the method of Refs. [17,26].

4. Zero-temperature reservoir

The fourth type of engineered reservoir was a zero-temperature reservoir realized by laser cooling. Some theoretical results for this reservoir were mentioned briefly in Section II A 1a. The experimental scheme is outlined in Fig. 9 and follows a proposal by Poyatos *et al.* [28]. The goal is to simulate decay of the states $|\downarrow\rangle|n\rangle$ into a $T = 0$ reservoir. To do this, we simultaneously drive on the first red sideband transitions $|\downarrow\rangle|n\rangle \rightarrow |\uparrow\rangle|n-1\rangle$ at a Rabi frequency Ω_{rsb} and the red-Doppler (D1 from Fig. 5) from $|\uparrow\rangle$ to the $P_{1/2}$ level at a rate Ω_D ($\ll \Gamma$). This is effectively a continuous Raman cooling process (in contrast to the step-wise Raman cooling process described at the end of Section III B) which eventually relaxes the system to a state in which all population is in the ground state $|0\rangle|\downarrow\rangle$ [29,30]. The $|\uparrow\rangle$ level is given an effective decay rate $\gamma_{\text{eff}} \sim \Omega_D^2/\Gamma$. We begin by preparing an initial state $|\downarrow\rangle(|0\rangle + |2\rangle)/\sqrt{2}$. The point of the experiment is to follow the time evolution of the coherence of this state ($\rho_{0\downarrow,2\downarrow}$ as we label the relevant off-diagonal element of the density matrix) as it decoheres during the cooling process. To gain a qualitative understanding of the experiment we can consider a reduced problem, as follows.

We are simulating a $T = 0$ reservoir by simultaneously driving (resonantly) on the red sideband and red-Doppler transitions. The red-Doppler drive gives the $|\uparrow\rangle$ state an effective linewidth γ_{eff} (see Fig. 9). The system density matrix obeys the following time evolution:

$$\dot{\rho} = i[\rho, H] + \frac{\gamma_{\text{eff}}}{2}[2\sigma_- \rho \sigma_+ - \sigma_+ \sigma_- \rho - \rho \sigma_+ \sigma_-] \quad (74)$$

with interaction-picture Hamiltonian

$$H = g(a^\dagger \sigma_- + a \sigma_+), \quad (75)$$

where $g \equiv \Omega_{\text{rsb}}$ is the Rabi rate of the red sideband drive (assumed real) and σ_+ (σ_-) is the raising (lowering) operator of the atom. Here we have neglected the effects of recoil heating, valid for $\eta^2 \ll 1$. This is simply the master equation for a driven, decaying two-state atom dressed by coupling to a harmonic oscillator system (familiar to cavity QED as the Jaynes-Cummings model [31] with atomic (but no cavity) decay). We consider the experiment in which we make an initial state

$$\psi_0 = |\downarrow\rangle(|0\rangle + |m\rangle)/\sqrt{2} \quad (76)$$

and we measure the coherence which we call $\rho_{m\downarrow,0\downarrow}$. Eq. 74 leads to:

$$\dot{\rho}_{m\downarrow,0\downarrow} = -i\sqrt{m}g\rho_{m-1\uparrow,0\downarrow} \quad (77)$$

$$\dot{\rho}_{m-1\uparrow,0\downarrow} = -i\sqrt{m}g\rho_{m\downarrow,0\downarrow} - \frac{\gamma_{\text{eff}}}{2}\rho_{m-1\uparrow,0\downarrow}. \quad (78)$$

The solution to this set of differential equations (with initial conditions specified by Eq. 76) is

$$\rho_{m-1\uparrow,0\downarrow} = \frac{-i\sqrt{m}g}{2(\lambda_+ - \lambda_-)} [e^{\lambda_+ t} - e^{\lambda_- t}] \quad (79)$$

$$\rho_{m\downarrow,0\downarrow} = \frac{1}{2(\lambda_+ - \lambda_-)} \left[(\lambda_+ + \frac{\gamma_{\text{eff}}}{2})e^{\lambda_+ t} - (\lambda_- + \frac{\gamma_{\text{eff}}}{2})e^{\lambda_- t} \right] \quad (80)$$

with

$$\lambda_{\pm} = -\frac{\gamma_{\text{eff}}}{4} \pm \frac{1}{2}\sqrt{\frac{\gamma_{\text{eff}}^2}{4} - 4mg^2}. \quad (81)$$

Consider two limiting cases. In the first, $g \gg \gamma_{\text{eff}}$, so that λ_{\pm} have an imaginary part. Here the time-evolution of the coherence is an exponentially decaying cosine, reflecting the fact that the coherent drive is faster than the decay rate:

$$\rho_{m\downarrow,0\downarrow}(t) \longrightarrow \frac{e^{-\gamma_{\text{eff}} t/4}}{2} \cos(\sqrt{m}gt). \quad (82)$$

In the second case $g \ll \gamma_{\text{eff}}$, so that λ_{\pm} are strictly real. In this case,

$$\rho_{m\downarrow,0\downarrow}(t) \longrightarrow \frac{1}{2} \exp\left(-m\frac{2g^2}{\gamma_{\text{eff}}}t\right), \quad (83)$$

and we have simple exponential decay of the off-diagonal density matrix element. It is instructive to compare this to the $T = 0$ limit of the amplitude reservoir presented in Section II A 1a. From Eq. 11 with $\rho_{om}(0) = 1/2$

$$\rho_{0m} = \frac{1}{2} \exp\left(-m\frac{\gamma}{2}t\right). \quad (84)$$

With the identification $\gamma/2 \rightarrow 2g^2/\gamma_{\text{eff}}$, Eqs. 83 and 84 are identical. This is the anticipated result, since the effective linewidth of the $|\uparrow\rangle$ state is simply the square of the Rabi frequency divided by the bare decay rate, and in the case of the red sideband the Rabi frequency scales as $g\sqrt{m}$.

IV. DATA

To reiterate, the experiments consist of a Ramsey type interferometer experiment in which the ion is coupled to one of the engineered reservoirs between the initial and final

“beam-splitter” pulses. The experiment proceeds as follows. The ion is first Doppler cooled and then Raman cooled, preparing the ion in the $|\downarrow\rangle|0\rangle$ state. The state preparation pulses are then applied to generate the desired superposition (first beam-splitter). A period of time elapses during which the ion is coupled to the reservoir. After this time, we reverse the sequence of pulses used in state preparation (second beam-splitter). The resulting internal state of the ion depends on the frequency and phase of the oscillators used in the preparation and reversal pulse sequences. The ion internal state is detected as described in Section III B. The contrast of the resulting Ramsey fringes is a measure of the motional state coherence, which decreases with increasing interaction with the reservoir, either in time or in strength (applied voltage noise).

A. Schrödinger cat decoherence

1. cat states, applied amplitude noise

The effect of coupling the Schrödinger-cat interferometer to the engineered amplitude reservoir is shown in Fig. 10. The reservoir is simulated by driving particular trap electrodes with a noisy potential V near the trap secular frequency as discussed in Section III D 1. The amplitude reservoir is coupled to the ion for $3\mu\text{s}$ between the beamsplitter pulses of the interferometer. The variance σ^2 of β (Section II B 2a) is proportional to the mean-squared voltage noise $\langle V^2 \rangle$. Fig. 10 shows a plot of the interference fringe contrast as a function of the applied mean squared voltage, scaled by the squared “size” of the cat state $|\Delta\alpha|^2$. Decay curves were recorded for a variety of superposition sizes $|\Delta\alpha|$, and all the data agree with a single exponential, as in Eq. 33. The initial contrast for each value of $|\Delta\alpha|$ is normalized to unity at $\langle V^2 \rangle = 0$.

2. cat states, natural noise

The natural noise that gives rise to the heating described in Section III D 3 causes decoherence. For this experiment, we simply wait for some amount of time between the Ramsey zones and measure the fringe contrast as a function of this time. The results are shown in Figure 11. As in the previous case, the results are consistent with a single exponential. This time, the decay constant has meaning relative to another experimental quantity: it should be the same as that measured for the heating. For example, the mean quantum number in the system is given by Eq. 8, from which γ is interpreted as the heating rate of Section III D 3. The decay constant relevant to the decoherence measured in Figure 11 is given by Eq. 73, with the same coupling constant γ appearing. The measured numbers for γ agree reasonably well. We find a decay rate of $\gamma/2\pi = 5.7 \pm 1$ quanta/ms from the heating data (Figure 8) and $\gamma/2\pi = 7.5 \pm 0.7$ quanta/ms from the decoherence data (Figure 11). Discrepancies can easily arise due to variations in heating rate from day to day and other systematic errors that are not included in the error quoted on γ , such as mis-calibration of the size of the coherent states $\Delta\alpha$. In addition, there is some spin decoherence during the $80\mu\text{s}$ of Ramsey time used for the longest data points which could account for some of the

discrepancy as well (see the discussion of Section II C). The contrast is normalized to unity at $t = 0$.

3. Cat states, phase noise

Results from coupling of the Schrödinger cat interferometer to the engineered phase reservoir are shown in Fig. 12. The theory has only one free parameter, which is a scaling to convert voltage noise to phase deviation (see below for a discussion of this). The theory curves are from Eq. 44, all with the same scaling parameter. Note that there is no simple universal scaling law for the functional form of the decoherence as there is in the case of Schrödinger cats subject to amplitude noise. The contrasts at $\langle V^2 \rangle = 0$ are normalized to unity. The phase noise reservoir is applied for $\sim 10 \mu\text{s}$.

B. Decoherence of superpositions of Fock states and decay of Fock states

1. Fock states, phase noise

Coupling the Fock state interferometer to phase noise results in the simple behavior predicted by Eq. 21. This is confirmed in the data of Figure 13 in which the fringe contrast of the interferometer is measured for different values of the applied phase noise reservoir. The data for different initial Fock state superpositions are scaled by the squared “size” $(\Delta n)^2$ of the superposition in order to show the universal scaling law of Eq. 21. The scaling of the x-axis of the graph is a free parameter in the theory. In principle, the size of the noise measured in radians could be known from the variance of the applied noise $\langle V^2 \rangle$. However, in practice, unknown geometrical factors in converting voltage on a subset of the trap electrodes to change in trap secular frequency prevents a direct comparison. A rough estimate, nonetheless, gives a correspondence of about π radians of phase noise at 0.1 V^2 , which is in rough agreement with the fit parameters from the data. The voltage noise was applied for a $10 \mu\text{s}$ interval.

2. Fock states, amplitude noise: decoherence and decay

The coupling of superpositions of Fock states to an amplitude reservoir is particularly relevant to quantum logic with trapped ions: Fock state superpositions are generated during quantum logic gates, and the natural decoherence is due to coupling to a hot thermal amplitude reservoir. Decoherence of superpositions of Fock states and heating (decay) of Fock states limit the fidelity of quantum operations.

a. decoherence To simplify analysis, we restricted our attention to superpositions of the form $(|0\rangle + |n\rangle)/\sqrt{2}$ in which Eq. 38 in Section II B 2b applies to a good approximation. Data for $n = 1, 2, 3$ are shown in Fig. 14, where the amplitude reservoir is the natural noise on the trap electrodes discussed in Section III D 3. Using Eq. 38 the fits F_n for states $(|0\rangle + |n\rangle)/\sqrt{2}$ are given by $F_n = \exp(-\gamma_s t)/(1 + s_n t)^{1+n}$ with s_n the scaling factor forced to be the same for all n . The exponential decay accounts for the loss of spin coherence due, for example, to

fluctuating magnetic fields, with $\gamma_s/2\pi \sim 0.01 \mu\text{s}^{-1}$. The best overall fit to the data gives $s_n = 5/\text{ms}$, which is consistent with the decay rates quoted in Section IV A 2.

b. decay of populations; purity and entropy In order to study this case more completely, we performed measurements directly on the populations (diagonal elements of the system density matrix). Starting from a Fock state $|n\rangle$, we applied the amplitude reservoir and observed the evolution of the system. The procedure was as follows. We generated the state $|n\rangle$ [17], waited a time t , during which the Fock state $|n\rangle$ would evolve to a distribution over Fock states $\{|n'\rangle\}$. We then drove transitions on the blue sideband (bsb) for various Raman probe times t_p . Following this, P_\downarrow was measured from the fluorescence signal. The resulting signal has contributions from all possible transitions $|\downarrow\rangle|n'\rangle \rightarrow |\uparrow\rangle|n'+1\rangle$, each of which is at a well-defined frequency. The bsb curve thus generated is described by:

$$P_\downarrow(t_p) = \frac{1}{2} + \sum_n \frac{1}{2} P_n [\cos(2\Omega_j t_p) e^{-\gamma_n t_p}] \quad (85)$$

with the Rabi frequency given by

$$\Omega_n = |\langle n|e^{-i\eta(a+a^\dagger)}|n+1\rangle| = \Omega_0 e^{-\eta^2/2} (n+1)^{-1/2} \eta \mathcal{L}_n^1(\eta^2), \quad (86)$$

where \mathcal{L} are Laguerre polynomials. The phenomenological decay rate $\gamma_n = -(n+1)^{0.7}\gamma_0$ is used to model decay in the data due to Raman beam intensity fluctuations and other sources [17]. We perform a singular value decomposition (svd) [32] on the data to extract the populations P_n of the various $|n\rangle$ -states at the end of the reservoir application time t . The time evolution of the populations is shown in Figure 15 for different initial starting states $\psi(0) = |n_0\rangle$. The theory curves are given in Eq. 10 which describe the evolution of the diagonals of the density matrix. From these data, the expected qualitative effects are evident. The theory for all the data of Figure 15 has only a single free parameter which is the scaling of the x-axis. Additionally, we use the svd populations from the initial experimental state for the initial state of the calculations ($\rho_{nn}(0)$ from Eq. 10).

An interesting way to further quantify the progression to thermal equilibrium of the system is via the purity and entropy of the (mixed) states. The time-evolution of the purity is shown in Figure 16 and of the entropy in Figure 17. It should be noted that we use the terms entropy and purity in an approximate sense: the svd is in practice only useful to $n \approx 4$, so we assign a cut-off to the calculations on the data. Additionally, only the diagonal elements $P_n \equiv \rho_{nn}$ are used. This is valid for initial Fock states and thermal states (to which the ground state evolves under the amplitude reservoir) since the coherences are absent. However, imperfections in state preparation could lead to unwanted coherences in the experimental states. In practice, we assume that such effects are small, but we have not experimentally verified this assumption. Some of the discrepancies between theory and data may result from this. The definitions under these constraints are, for the purity,

$$\mathcal{P}(t) \equiv \text{Tr}\rho^2(t) \simeq \sum_{n=0}^{n_{\max}} P_n^2(t) \quad (87)$$

and for the entropy,

$$\mathcal{S}(t) \equiv \text{Tr}\rho(t) \log \rho(t) \simeq \sum_{n=0}^{n_{\max}} P_n(t) \log P_n(t) \quad (88)$$

where n_{\max} is the value of n at which the series is truncated. As stated above, since preparation of individual Fock states is not perfect, it is necessary to take into account the imperfections in the initial state populations, especially as the initial state gets large. To match the data to the theory, the initial diagonal elements of the density matrix are measured and used as an initial condition in the theory curves. The theory that is compared to the data is also truncated at n_{\max} . This has only a minor effect on the purity calculation, but does change the qualitative result of the entropy, which for a limited basis set saturates much more quickly and to a lower value than it otherwise would. The predicted entropy and purity curves (with no truncation, that is, as $n_{\max} \rightarrow \infty$) are shown as the dotted lines in their respective figures.

C. Zero-temperature reservoir

c. Decoherence Here we discuss the effect of the variable-bandwidth zero-temperature reservoir presented in Section IIID 4 on a superposition of Fock states. As before, we prepare the superposition state, apply the reservoir, and undo the state preparation forming a Ramsey interferometer to measure the coherence. In this case, the only state considered was the superposition state $|\downarrow\rangle[|0\rangle + |2\rangle]/\sqrt{2}$.

We distinguish the two limiting cases discussed in Section IIID 4. In the first, the effective decay rate γ_{eff} is much faster than the coherent Rabi rate Ω_{rsb} . This regime leads to exponential decay of the coherence and is a simulation of a broad bandwidth $T = 0$ reservoir. In the other, the effective decay rate is slow compared to the coherent Rabi rate. Here, the system is driven coherently before appreciable decay sets in. Thus the coherent drive (on the rsb) is capable of completing several Rabi oscillations of the spin. The evolution of fringe contrast shows that the coherence goes to zero (as a π pulse transfers most of the population out of $|\downarrow\rangle|2\rangle$ into $|\uparrow\rangle|1\rangle$ and therefore destroys all coherence between $|2\rangle$ and $|0\rangle$) but then comes back (with opposite sign) as a reservoir pulse with area greater than π is applied. During this time, the coherence is decaying due to dissipation on $|\uparrow\rangle$. The evolution between the two regimes is shown in Figure 18. Note that the first graph has almost no decay. Here the red Doppler was absent ($\gamma_{\text{eff}} \propto \Omega_D = 0$) so that the residual decay is dominated by natural heating and Rabi frequency fluctuations. In the subsequent graphs, either the strength of the red Doppler laser, or the Rabi frequency of the rsb drive, or both were changed in such a way as to increase the ratio of dissipation to coherent drive, $\gamma_{\text{eff}}/\Omega_{\text{rsb}}$.

The experiment has an additional parameter that must be accounted for. The application of the Red Doppler beam causes a Stark shift of the level $|\uparrow\rangle$. In the data of Figure 18 this effect was corrected for during the experiment simply by changing the detuning of the Raman beams to compensate for the level shift; this must be done anew for each value of Ω_{rsb} . It is more convenient to perform the experiment not compensating for the Stark shift Δ . The theory for this is only slightly more complicated than that associated with Eq. 80, which can be generalized to:

$$\rho_{m\downarrow,0\downarrow} = \frac{1}{2} \exp(-\gamma_{\text{eff}}t/4) \left[\cos \frac{\Omega_R t}{2} - i \frac{\tilde{\Delta}}{\Omega_R} \sin \frac{\Omega_R t}{2} \right] \quad (89)$$

$$\tilde{\Delta} = \Delta + \frac{i\gamma_{\text{eff}}}{2} \quad (90)$$

$$\Omega_R = \sqrt{4mg^2 + \tilde{\Delta}^2}. \quad (91)$$

A progression of increasing $\gamma_{\text{eff}}/\Omega_R$ with Stark-shift detunings is shown in Figure 19.

d. Decay For completeness, we also consider the decay subject to the zero temperature reservoir of the diagonals of the density matrix (with no detunings, $\Delta = 0$). We measure the time-evolution of these populations starting from an initial state of $\psi(0) = |\downarrow\rangle|2\rangle$. The predicted time-evolution is given by Eq. 12. The data are shown in Figure 20. One will immediately notice the negative “populations.” This results from population left in the $|\uparrow\rangle$ state after the continuous Raman cooling. For weak enough Red Doppler, the optical pumping does not entirely depump the $|\uparrow\rangle$ state. This appears as a negative contribution to the flopping state analysis seen in the first two panels of Fig. 20 (see Eq. 85).

V. CONCLUSION

We have presented a detailed study of the interaction of several types of quantum states with several types of engineered reservoirs. The results compare favorably with theoretical predictions, and for several cases, we have confirmed predicted scalings for a range of experimental conditions.

We acknowledge support from the U. S. National Security Agency, Office of Naval Research and Army Research Office. We thank Chris Langer, Mary Rowe, Mike Lombardi, and Don Sullivan for critical readings of the manuscript.

* Work of an agency of the US government. Not subject to US copyright.

** electronic mail: quentint@boulder.nist.gov.

*** Present address: Research Electro-Optics, Boulder, CO.

**** present address: NIST, Gaithersburg, MD.

- [1] W.H. Zurek, Phys. Today, **44** (Oct.), 36 (1991), and references therein.
- [2] A.O. Caldeira and A.J. Leggett, Phys. Rev. A **31**, 1059 (1985).
- [3] D.F.Walls and G.J.Milburn, Phys. Rev. A **31**, 2403 (1985).
- [4] M. Collett, Phys. Rev. A **38**, 2233 (1988).
- [5] H.J. Carmichael *An open systems approach to Quantum Optics*, Springer-Verlag (Berlin:1993).
- [6] C.W. Gardiner, *Quantum Noise*, Springer-Verlag (Berlin: 1991).
- [7] D.F.Walls and G.J.Milburn, *Quantum Optics*, (Springer-Verlag, Berlin, 1994).
- [8] V. Bužek and P. L. Knight in *Progress in Optics XXXIV*, Elsevier (Amsterdam:1995), pp 1-158.
- [9] J. I. Cirac and P. Zoller, Phys. Rev. Lett. **74**, 4091 (1995).
- [10] C. Monroe, D.M. Meekhof, B.E. King, and D.J. Wineland, Science **272**, 1131 (1996).
- [11] M. Brune, E. Hagley, J. Dreyer, X. Maître, A. Maali, C. Wunderlich, J.M. Raimond, and S. Haroche, Phys. Rev. Lett. **77**, 4887 (1996).

- [12] C.J. Myatt, B.E. King, Q.A. Turchette, C.A. Sackett, D. Kielpinski, W.M. Itano, C. Monroe, D. J. Wineland, *Nature* **403**, 269 (2000).
- [13] V. Peřinová and A. Lukš, *Phys. Rev. A* **41**, 414 (1990).
- [14] M.S. Kim and V. Bužek *Phys. Rev. A* **46**, 4239 (1992).
- [15] C.J. Myatt, et al., ICOLS (2000) (unpublished).
- [16] D.J. Wineland, C. Monroe, W.M. Itano, D. Leibfried, B.E. King, and D.M. Meekhof, *J. Res. NIST* **103**, 259 (1998).
- [17] D.M. Meekhof, C. Monroe, B.E. King, W.M. Itano, and D.J. Wineland, *Phys. Rev. Lett.* **76**, 1796 (1996).
- [18] C. Monroe, D.M. Meekhof, B.E. King, S.R. Jefferts, W.M. Itano, D.J. Wineland, and P. Gould, *Phys. Rev. Lett.* **75**, 4011 (1995).
- [19] S. Wallentowitz and W. Vogel, *Phys. Rev. A* **58**, 679 (1998).
- [20] W.M. Itano, C. Monroe, D.M. Meekhof, D. Leibfried, B.E. King, and D. J. Wineland, *SPIE Proc.* **2995**, 43 (1997).
- [21] M.G. Raizen, J.M. Gilligan, J.C. Bergquist, W.M. Itano, and D. J. Wineland, *Phys. Rev. A* **45**, 6493 (1992).
- [22] S.R. Jefferts, C. Monroe, E.W. Bell, and D.J. Wineland, *Phys. Rev. A* **51**, 3112 (1995).
- [23] B.E. King, PhD thesis, University of Colorado (1999).
- [24] Q. A. Turchette, C. S. Wood, B. E. King, C. J. Myatt, D. Leibfried, W. M. Itano, C. Monroe, D. J. Wineland, *Phys. Rev. Lett.* **81**, 3631 (1998).
- [25] D. J. Wineland, C. Monroe, W. M. Itano, B. E. King, D. Leibfried, D. M. Meekhof, C. Myatt, C. Wood, *Fortschr. Phys.* **46**, 363 (1998).
- [26] Q. A. Turchette, C. S. Wood, B. E. King, C. J. Myatt, D. Leibfried, W. M. Itano, C. Monroe, D. J. Wineland, quant-ph/0002040 (unpublished).
- [27] B. E. King, C. S. Wood, C. J. Myatt, Q. A. Turchette, D. Leibfried, W. M. Itano, C. Monroe, D. J. Wineland, *Phys. Rev. Lett.* **81**, 1525 (1998).
- [28] J.F. Poyatos, J.I. Cirac, and P. Zoller, *Phys. Rev. Lett.* **77**, 4728 (1996).
- [29] F. Dietrich, J. C. Bergquist, W.M. Itano, D.J. Wineland, *Phys. Rev. Lett.* **62**, 403 (1989).
- [30] I. Marzoli, J.I. Cirac, R. Blatt, P. Zoller, *Phys. Rev. A* **49**, 2771 (1994).
- [31] E. T. Jaynes and F. W. Cummings, *Proc. IEEE* **51**, 89 (1963).
- [32] W.H. Press, S.A. Teukolsky, W.T. Vetterling, B.P. Flannery, *Numerical Recipes in C*, Cambridge Univ. Press (New York: 1996).

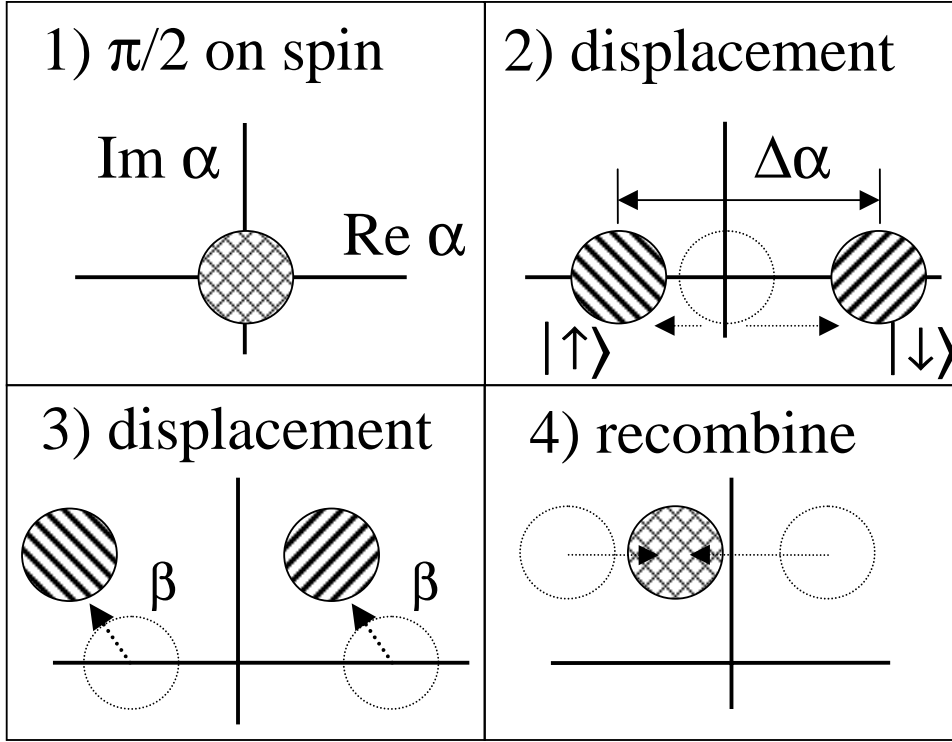


FIG. 1. Pictorial representation of the Schrodinger cat interferometer with coupling to an amplitude reservoir. The coherent states are represented by minimum uncertainty circles in phase space, while the different spin states are indicated by the hatching. In panel 1, a spin superposition $|\psi\rangle = (|\downarrow\rangle + |\uparrow\rangle)|0\rangle/\sqrt{2}$ is created with a $\pi/2$ pulse on the carrier transition. The cat state $|\psi\rangle = (|\downarrow\rangle|\alpha_\downarrow\rangle + |\uparrow\rangle|\alpha_\uparrow\rangle)/\sqrt{2}$ is completed with a spin dependent dipole force, as shown in panel 2. The effects of coupling to an engineered amplitude reservoir are shown in panel 3. A random displacement by β in panel 3 displaces both spin states equally, but with different phase factors. After the reversal of the initial displacement in panel 4 the motion may again be factored out, but leaving a relative phase shift $2\text{Im}\beta\Delta\alpha^*$ between the spin components. An ensemble average over β leads to a loss of contrast (decoherence) that scales with the size of the superposition, $|\Delta\alpha|$.

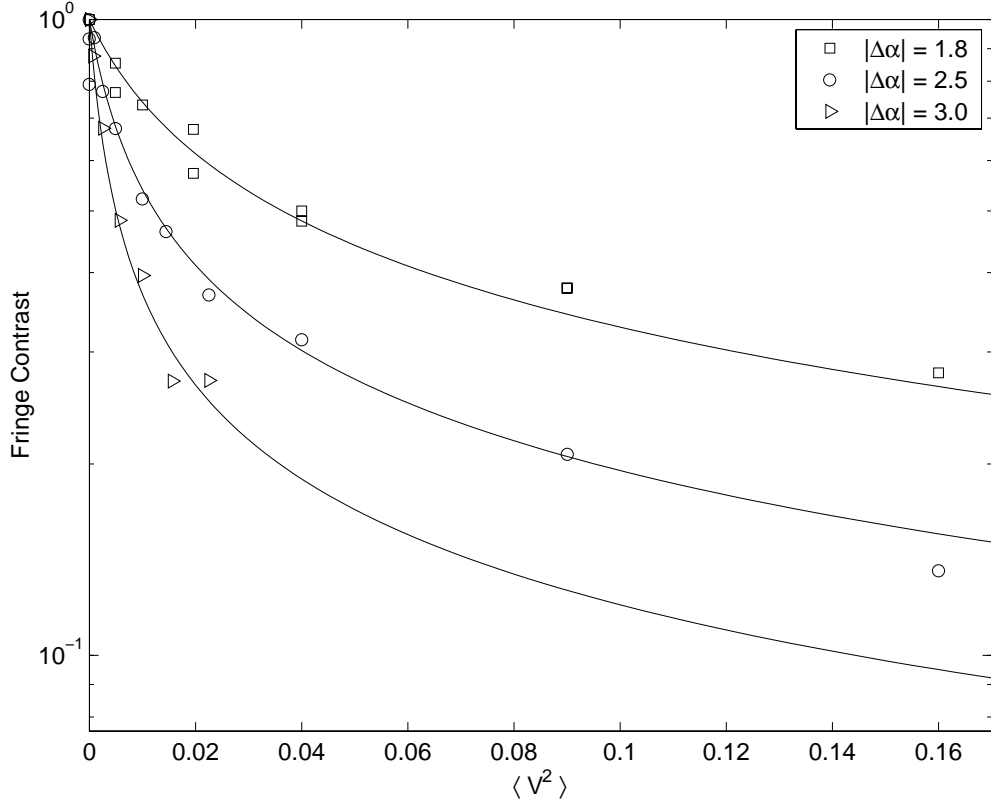


FIG. 2. Pictorial representation of the Schrodinger-cat interferometer with coupling to a phase reservoir. The coherent states are represented by minimum uncertainty circles in phase space, while the different spin states are indicated by the hatching. In panel 1, a spin superposition $|\psi\rangle = (|\downarrow\rangle + |\uparrow\rangle)|0\rangle/\sqrt{2}$ is created with a $\pi/2$ pulse on the carrier transition. The cat state $|\psi\rangle = (|\downarrow\rangle|\alpha_\downarrow\rangle + |\uparrow\rangle|\alpha_\uparrow\rangle)/\sqrt{2}$ is completed with a spin dependent dipole force, as shown in panel 2. Coupling to a phase reservoir is depicted in panel 3. The random phase shift in panel 3 prevents the correct reversing of the initial creation of the cat, resulting in a loss of contrast due to both the phase shift ϕ as well as the reduced spatial overlap.

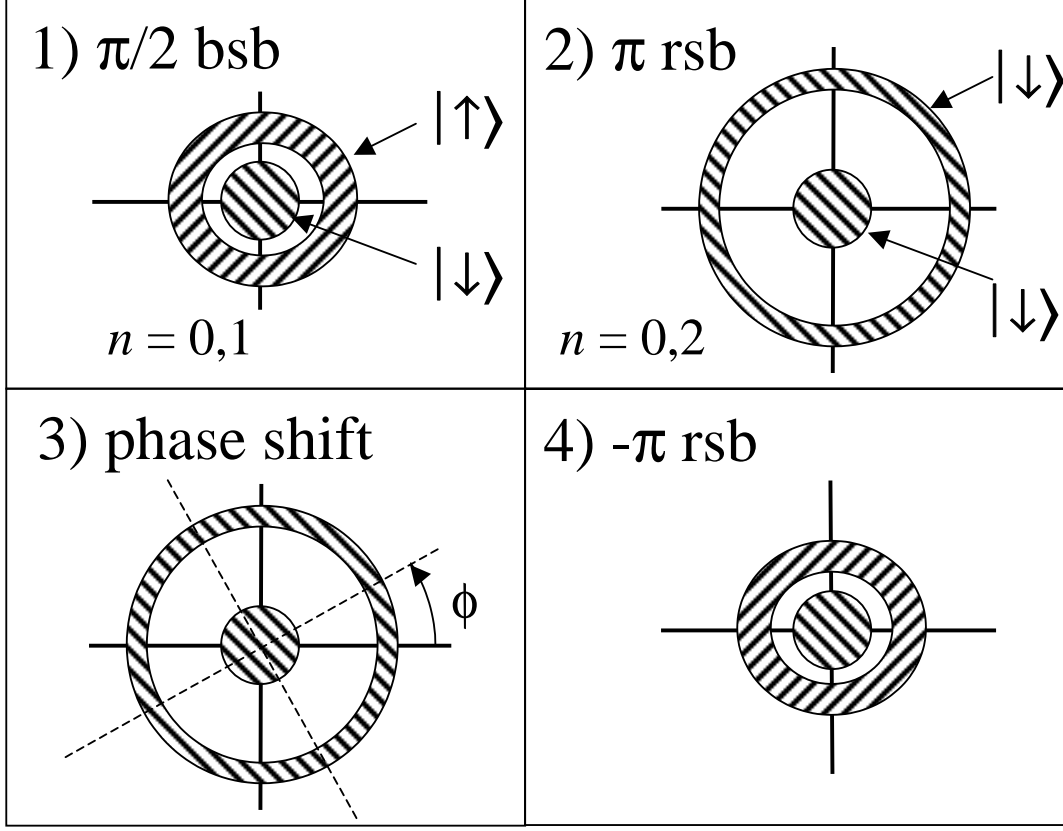


FIG. 3. Pictorial representation of the action of a phase reservoir on a Fock state interferometer. Here we consider the interferometer that generates the state $|\psi\rangle = |\downarrow\rangle(|0\rangle + |2\rangle)/\sqrt{2}$. A $\pi/2$ pulse on the first blue sideband generates the state $|\psi\rangle = (|\downarrow\rangle|0\rangle + |\uparrow\rangle|1\rangle)/\sqrt{2}$ depicted in panel 1, where the different spin states are indicated by the shading. A π pulse tuned to the first red sideband drives the transition $|\uparrow\rangle|1\rangle \rightarrow |\downarrow\rangle|2\rangle$ and generates the desired superposition. The random motional phase shift ϕ in panel 3 adds a relative phase factor, $|\psi\rangle = |\downarrow\rangle(|0\rangle + e^{-2i\phi}|2\rangle)/\sqrt{2}$, where the phase is scaled by the difference in indices of the Fock states (2 in this case). A second π pulse generates the state $|\psi\rangle = (|\downarrow\rangle|0\rangle + e^{-2i\phi}|\uparrow\rangle|1\rangle)/\sqrt{2}$ (panel 4). The result of the final $\pi/2$ pulse depends on the phase ϕ . Random fluctuations in ϕ result in decreased contrast of the Ramsey fringes.

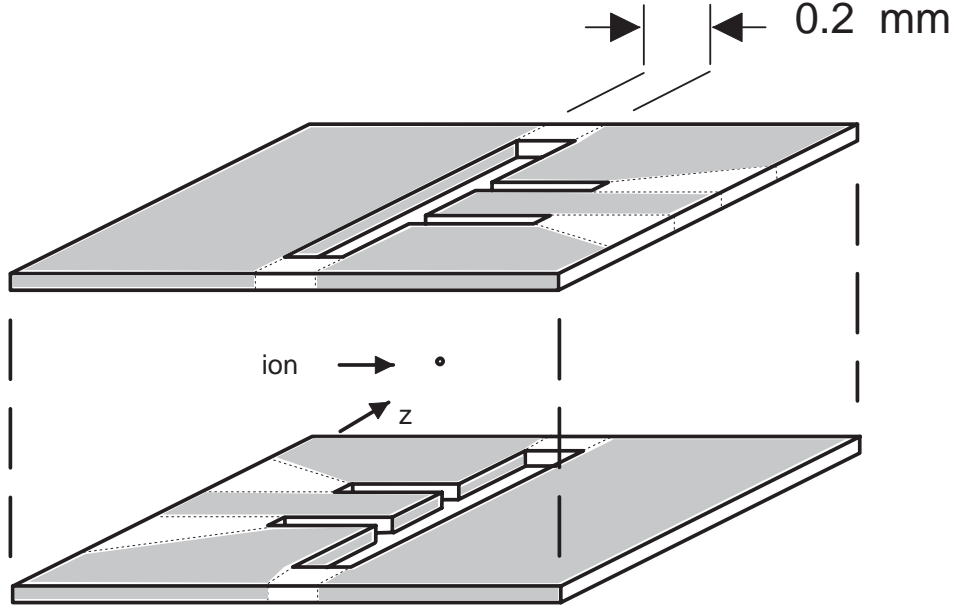


FIG. 4. Schematic diagram of the electrodes of the linear trap (not to scale). The trap electrodes are formed by evaporating gold onto alumina substrates. The outer segmented electrodes are the endcaps, while the long unbroken electrodes carry rf. The axial (\hat{z}) direction is parallel to the rf electrode. The two separate trap wafers are separated by $200\ \mu\text{m}$ with alumina spacers (not shown).

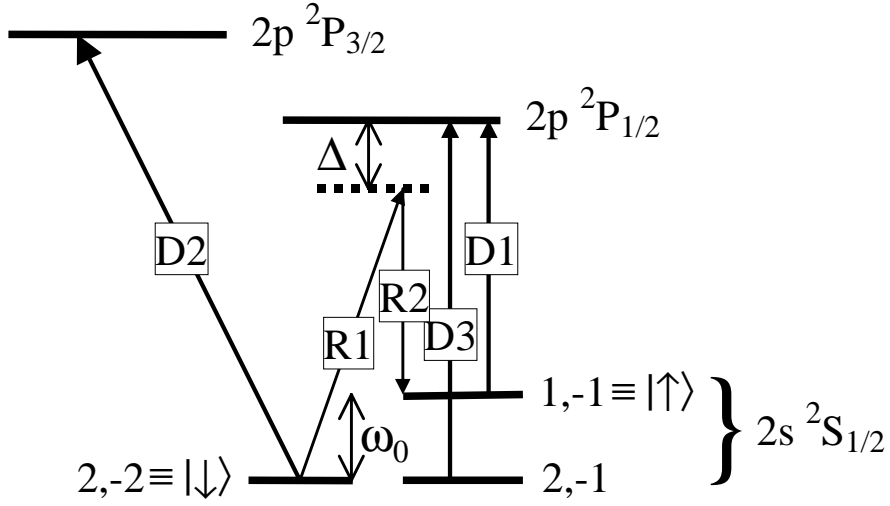


FIG. 5. Simplified level diagram of ${}^9\text{Be}^+$ (not to scale). The transitions labeled D are: D1: optical pumping (also called red Doppler), D2: detection/cooling, D3: repumping. The transitions labeled R are the two arms of the two-photon stimulated-Raman transition. Δ is the detuning between the $2p \ ^2P_{1/2}$ and the Raman virtual level and $\omega_0/2\pi = 1.25$ GHz is the $2s \ ^2S_{1/2}$ hyperfine splitting. The fine-structure splitting of the P-state is 197 GHz. The transition wavelength from the S to P state is 313 nm.

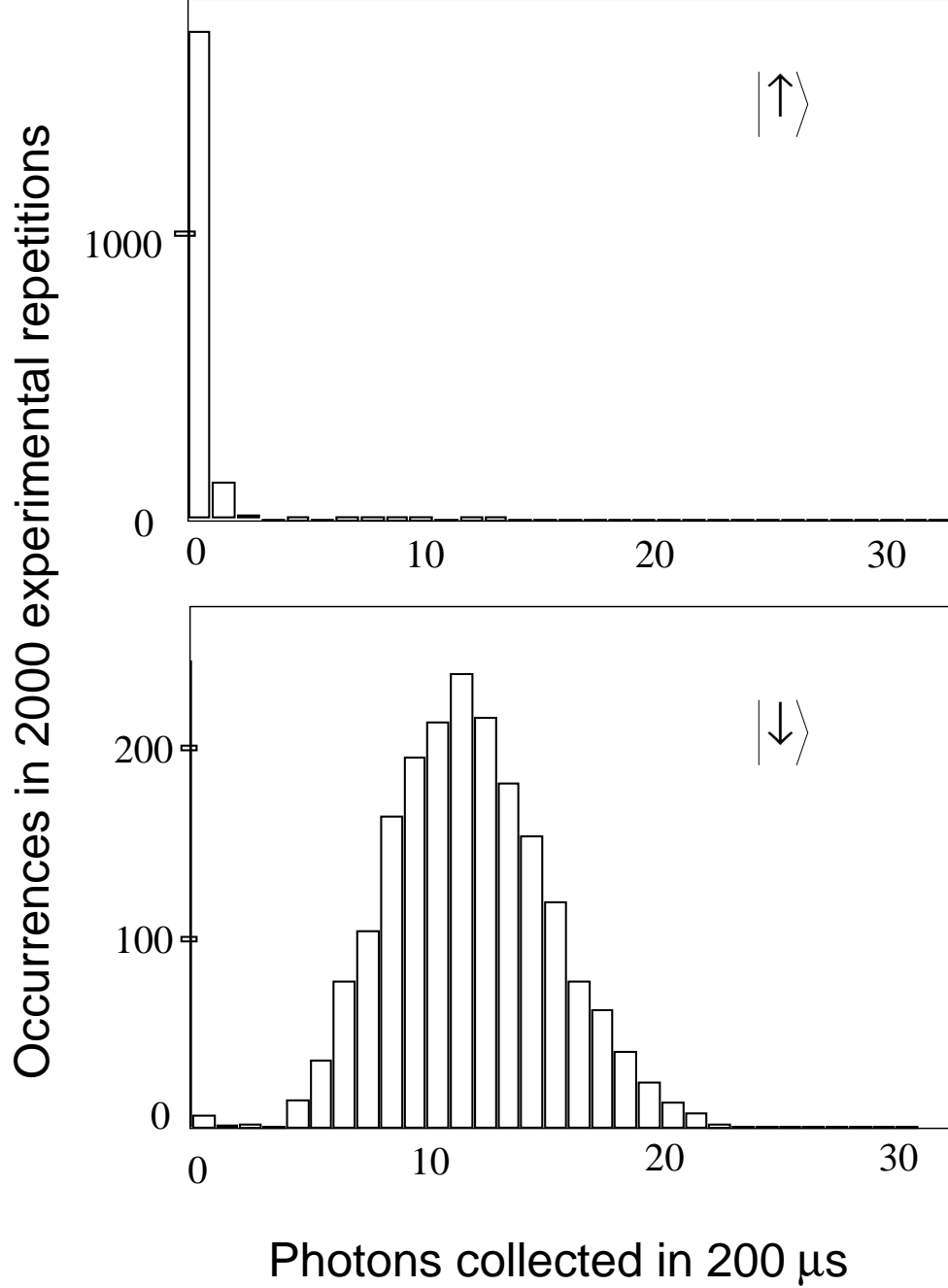


FIG. 6. Detection efficiency. The graphs show histograms of photons collected in a 200 μ s interval for 2000 repetitions of the experiment for the two initial states $|\downarrow\rangle$ and $|\uparrow\rangle$. Note that if a discriminator were placed at the bin associated with $n = 3$ photons, then, *on a per experiment basis*, the state of the ion would be distinguishable with a 97% quantum efficiency.

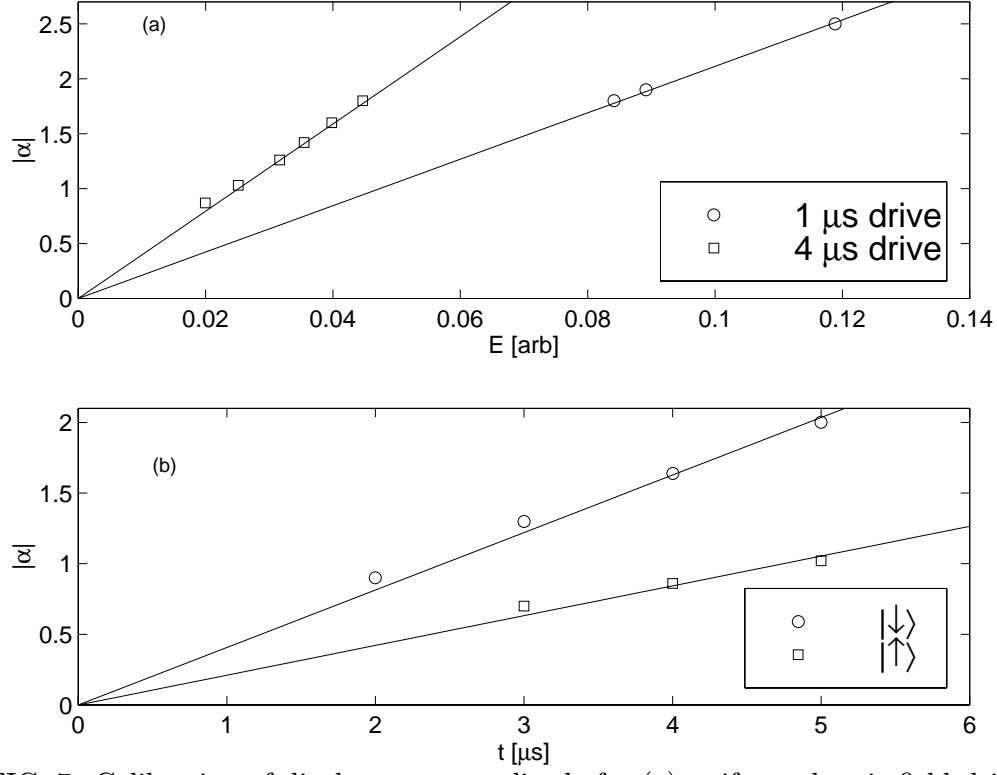


FIG. 7. Calibration of displacement amplitude for (a) uniform electric-field drive and (b) laser drive. The y-axis is in terms of the coherent-state amplitude α , determined as described in the text.

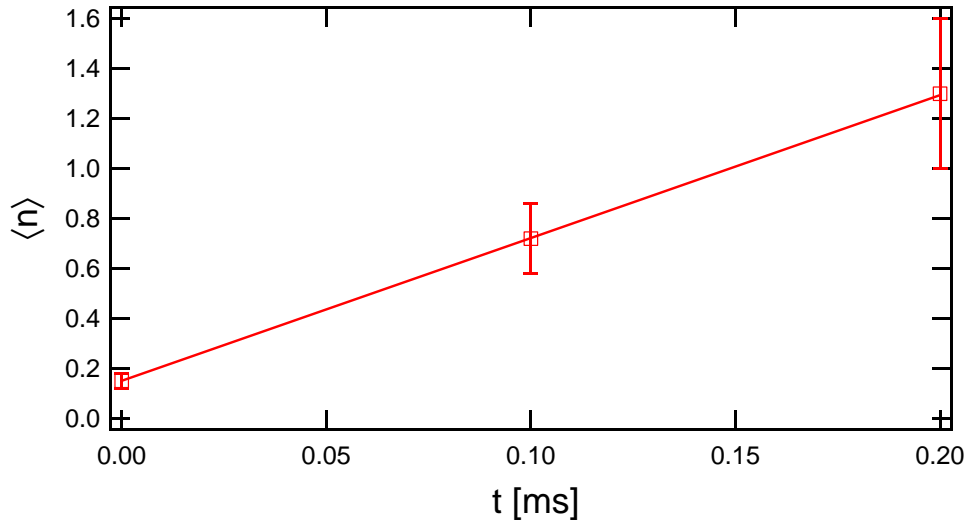


FIG. 8. Heating of the motional state. At $t = 0$ the ion is prepared in a state near the ground state $|0\rangle$. As time passes, the ion heats out of the ground state, as measured by the energy in the motional state which is proportional to the average occupation number $\langle n \rangle$.

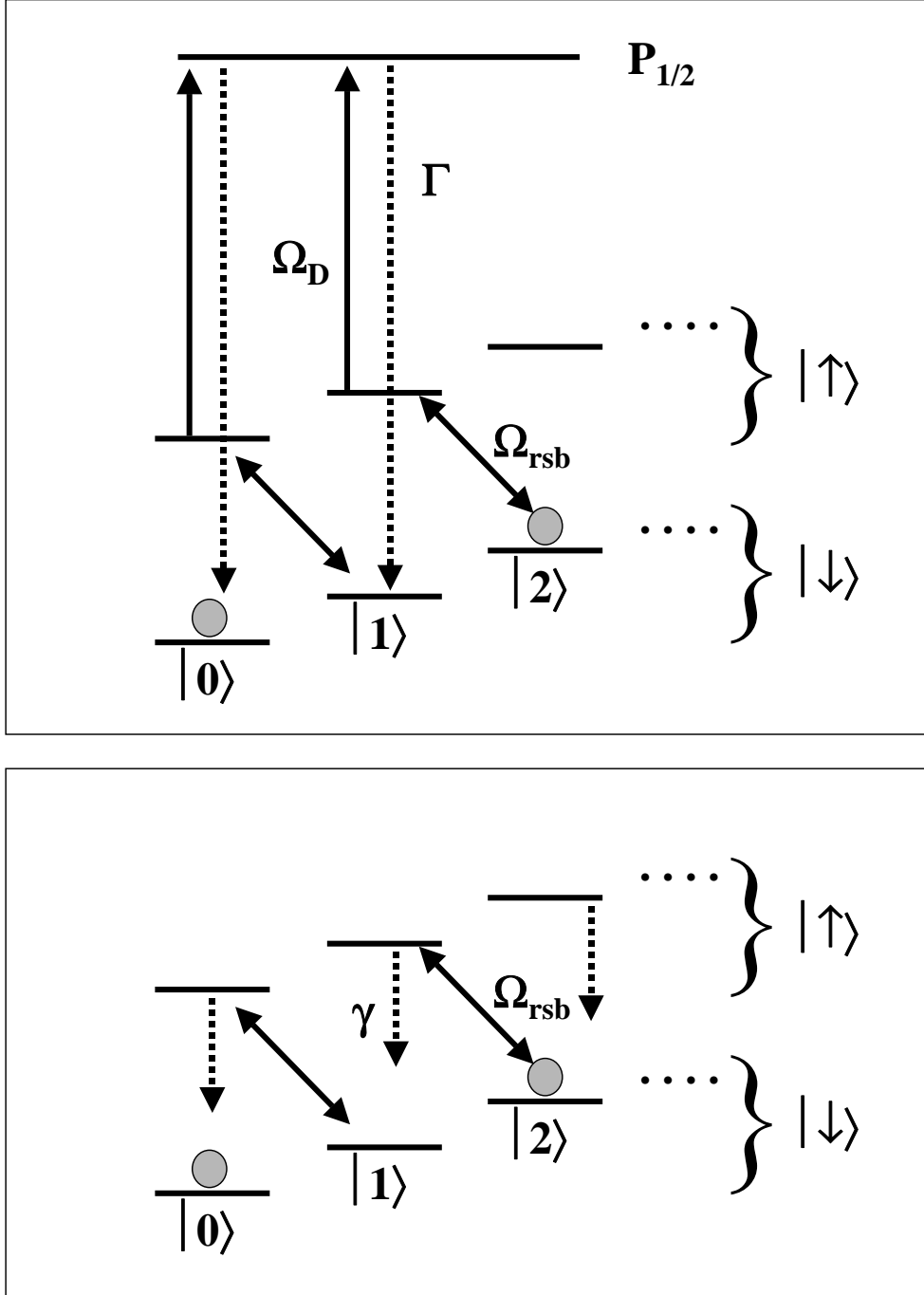


FIG. 9. Engineering a $T = 0$ reservoir with laser cooling: schematic diagram of the levels. The top panel shows the full three-(internal) level system (dressed by the motional states), while the bottom panel shows the equivalent two-level system. The red Doppler beam with resonant Rabi frequency Ω_D is used to give the $|\uparrow\rangle$ state an effective linewidth $\gamma \equiv \gamma_{\text{eff}} \approx \Omega_D^2/\Gamma$. Simultaneously the red sideband (rsb) is driven coherently at rate Ω_{rsb} to drive population out of the $|\downarrow\rangle$ state. The sum of the two applied fields simulates a variable bandwidth zero temperature reservoir.

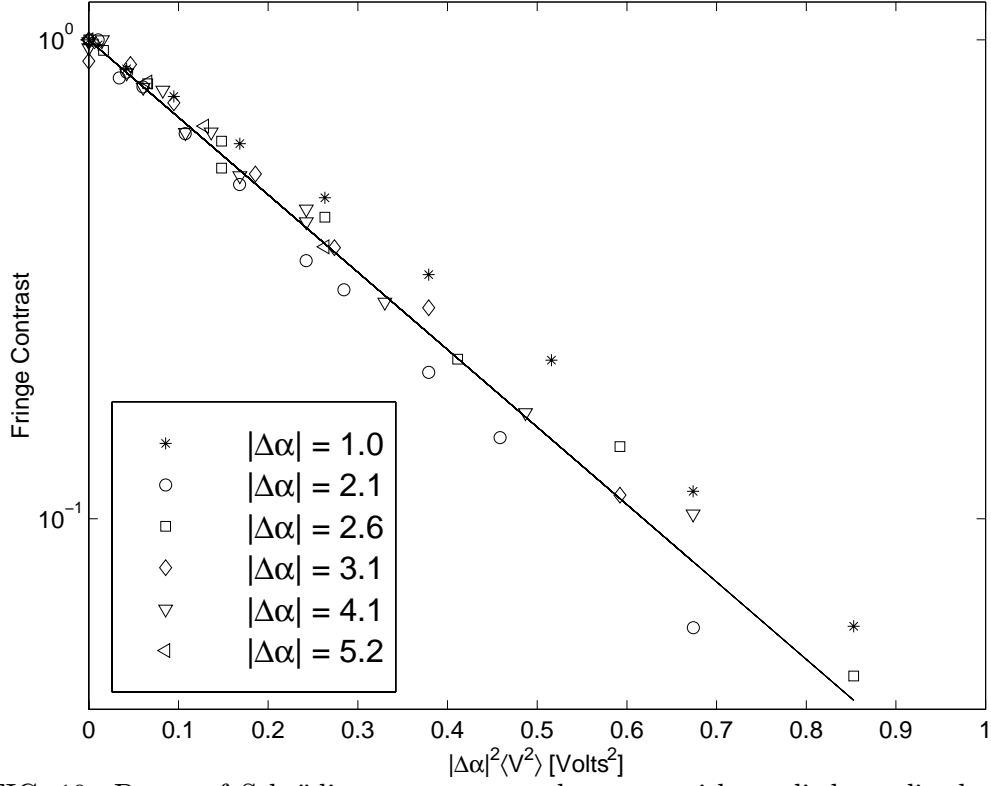


FIG. 10. Decay of Schrödinger cat state coherences with applied amplitude noise. Note the universal scaling of the states to an exponential with decay constant proportional to $|\Delta\alpha|^2$. The reservoir was applied for $3 \mu\text{s}$.

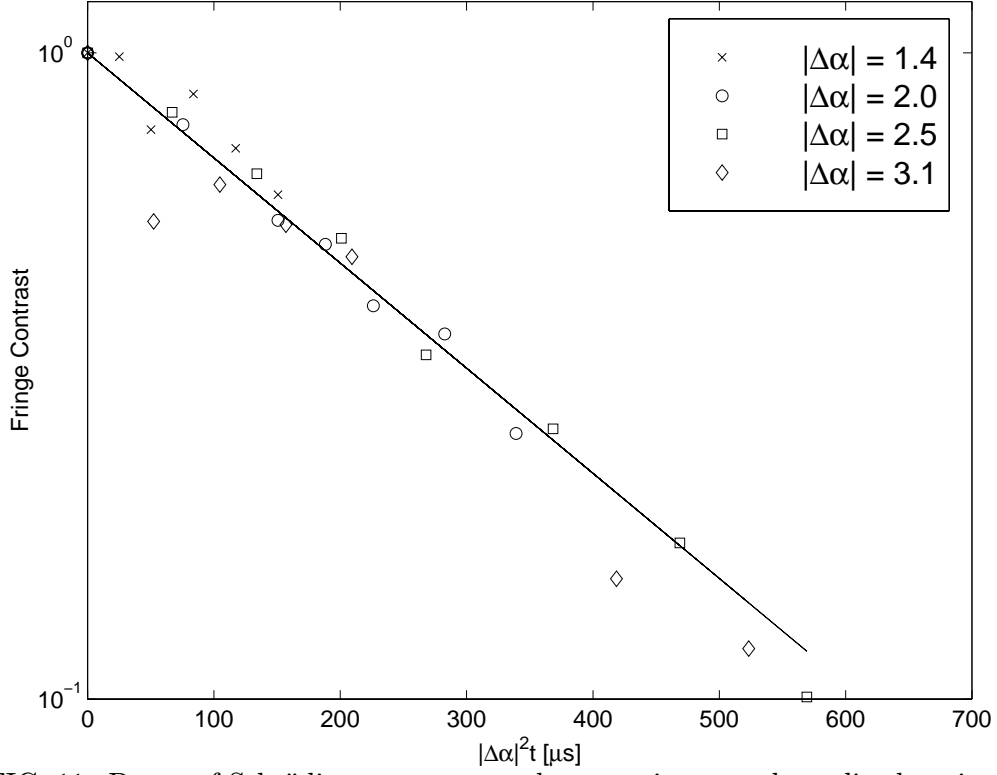


FIG. 11. Decay of Schrödinger cat state coherences in natural amplitude noise. Note again the universal scaling of the states to an exponential with decay constant proportional to $|\Delta\alpha|^2$, and that the decay constant is the same as that derived from the heating data of Figure 8. This is discussed further in the text.

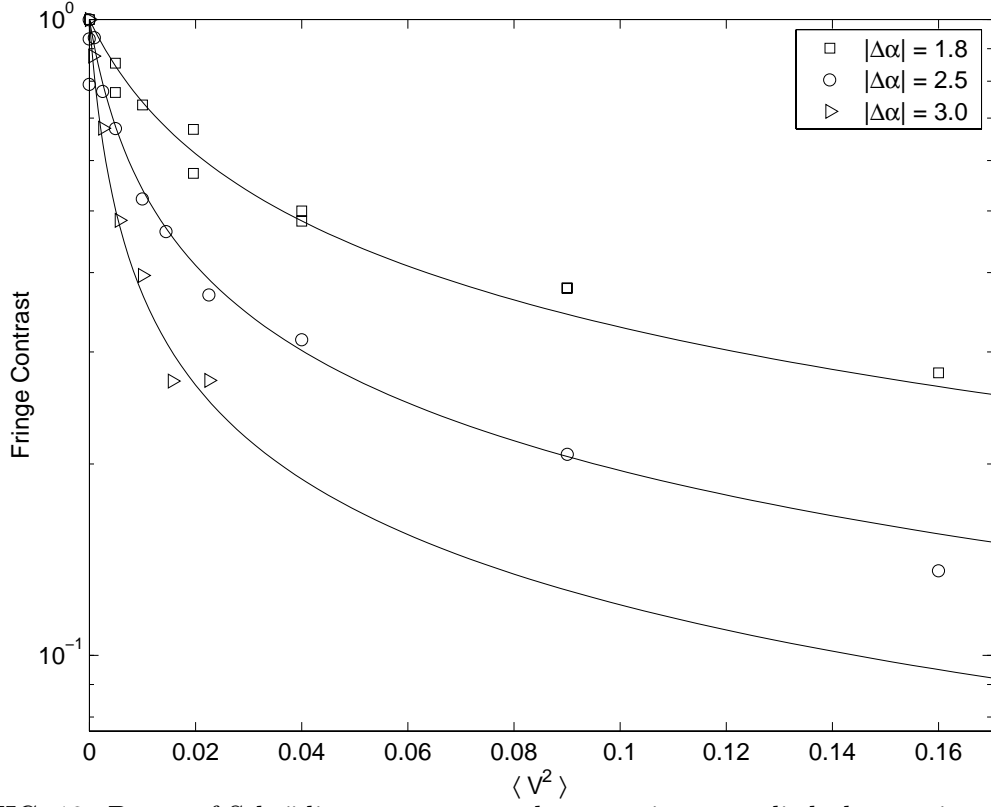


FIG. 12. Decay of Schrödinger cat state coherences in an applied phase noise reservoir. Several sizes of cats are shown. The reservoir was applied for $20 \mu s$.

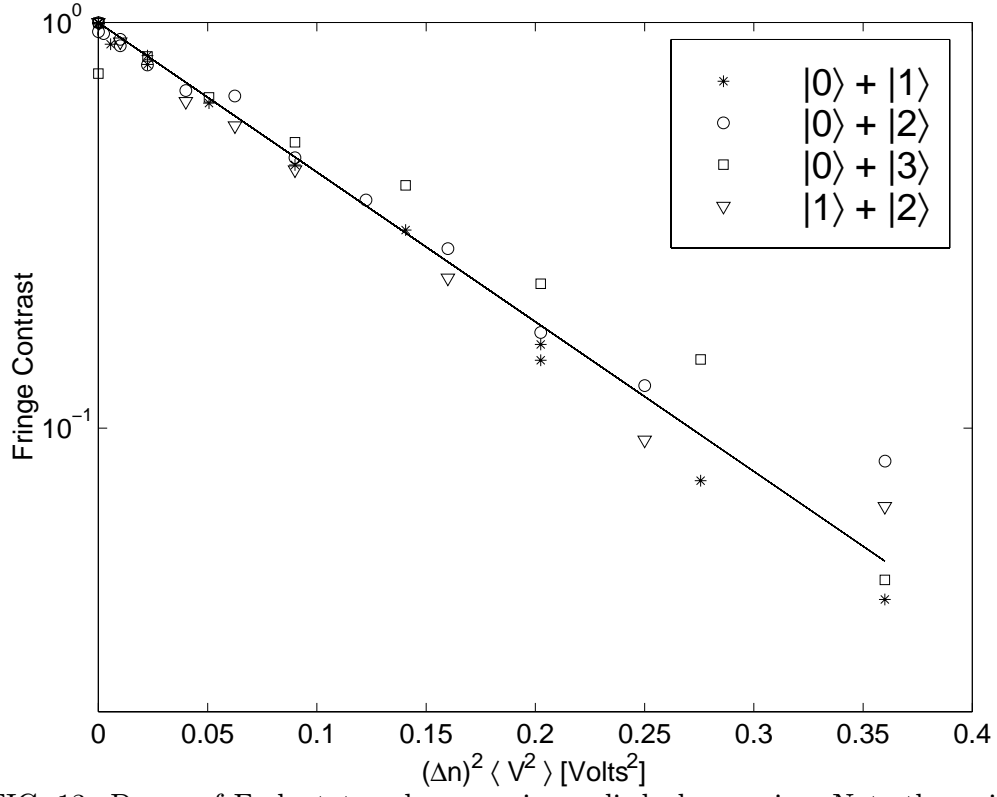


FIG. 13. Decay of Fock state coherences in applied phase noise. Note the universal scaling of the states to an exponential with decay constant proportional to $|\Delta n|^2$. The reservoir was applied for $10 \mu s$.

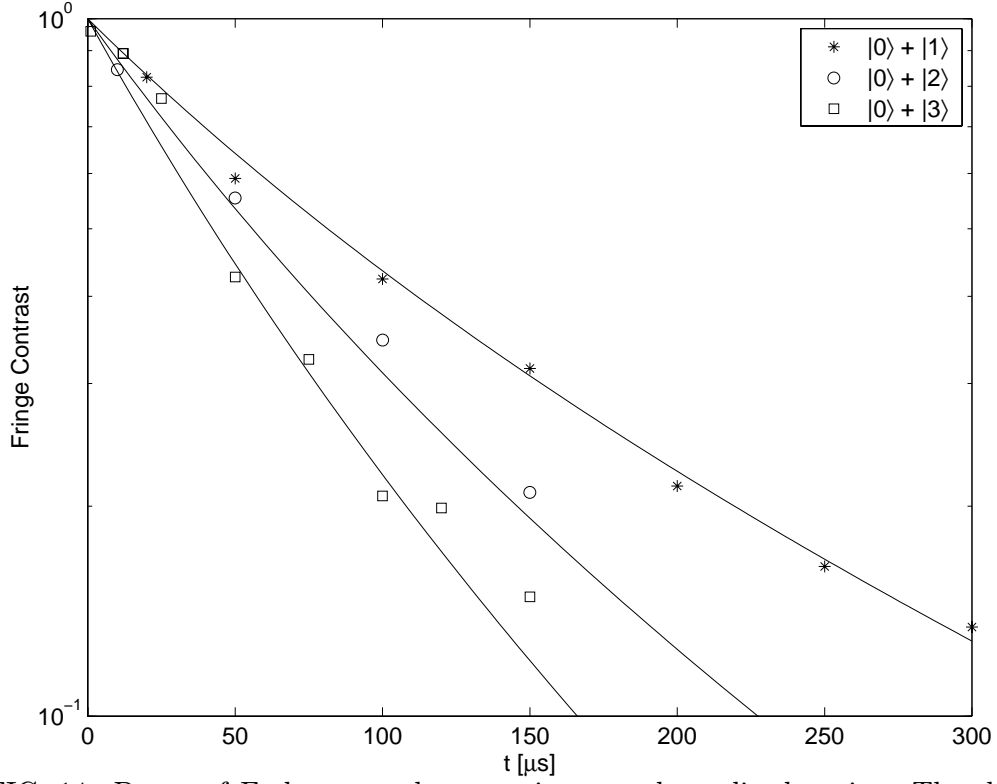


FIG. 14. Decay of Fock state coherences in natural amplitude noise. The theory curves are to the functional form of Equation 38 with an additional exponential decay to account for spin decoherence. The horizontal scaling is forced to be the same for the three states, and the data are normalized to unit contrast at $t = 0$.

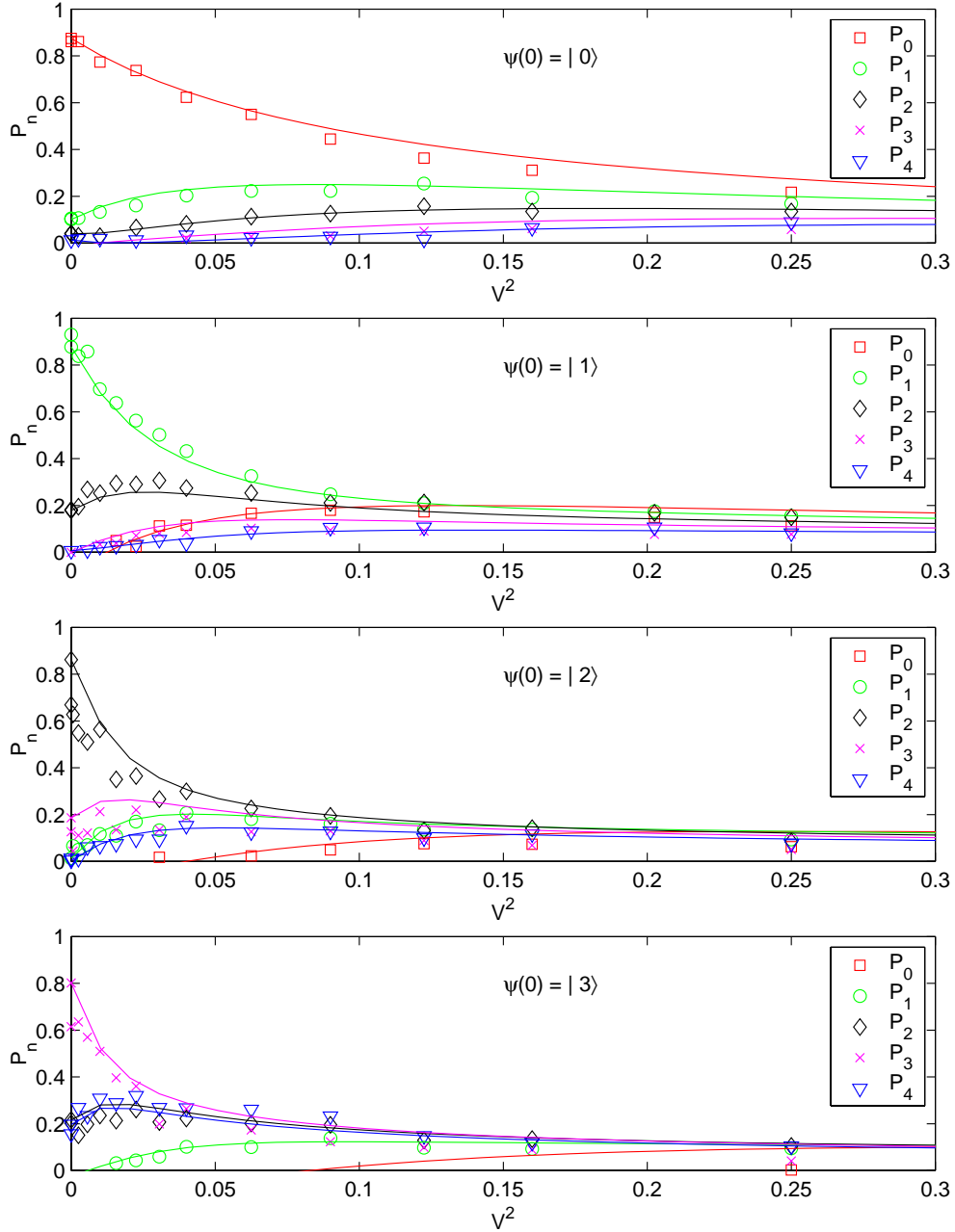


FIG. 15. Decay of Fock states in a hot amplitude reservoir. Each graph shows the time evolution of the populations P_n in state $|n\rangle$ of the motional state for an experiment starting in the initial state $\psi(0)$ indicated. (The initial states are not perfectly generated, as can be seen by $P_n(0)$.) The populations are given in Eq. 10, from which the solid lines are derived.

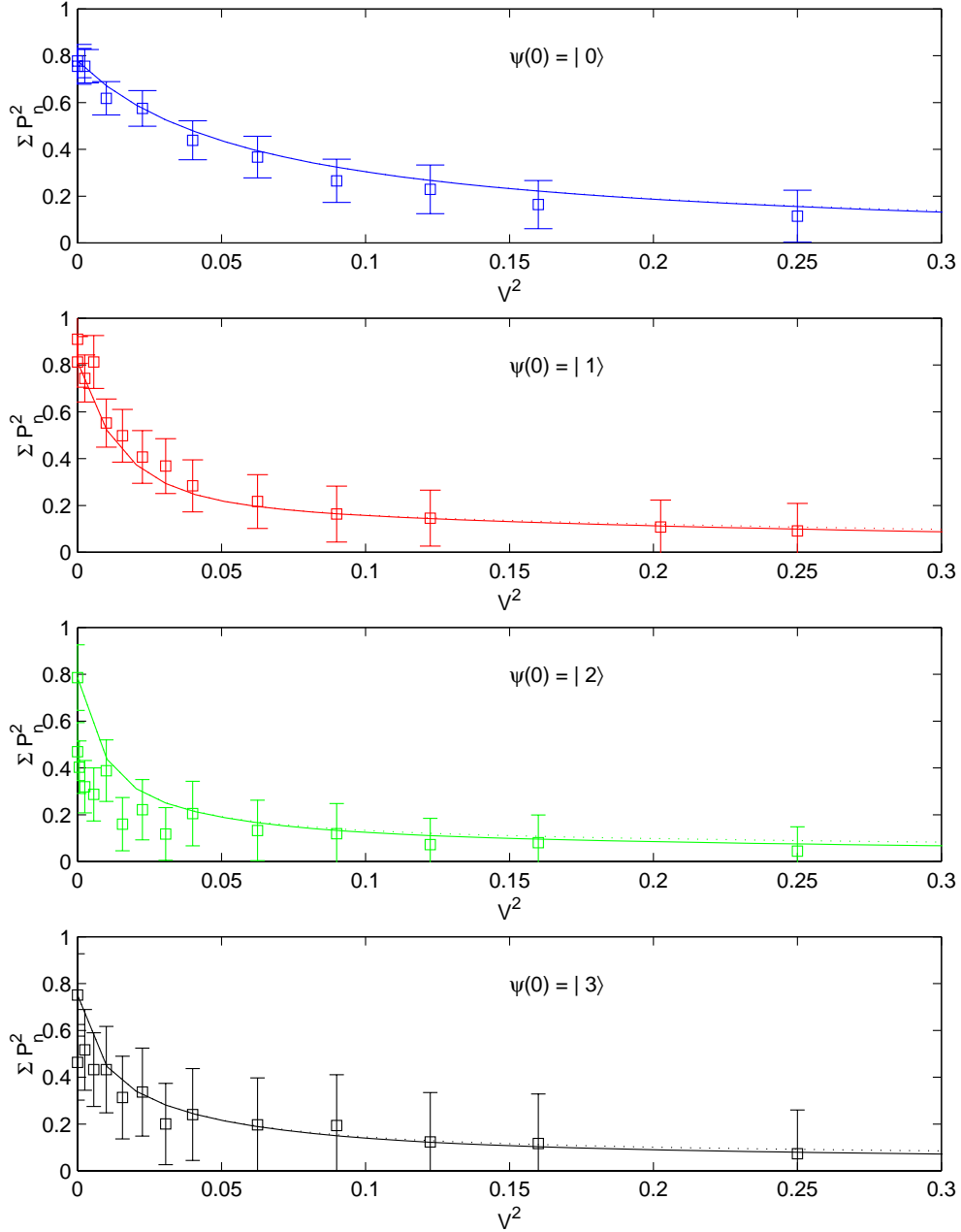


FIG. 16. Evolution of purity for initial Fock states in hot amplitude reservoir. Each graph shows the time evolution of the purity of the motional state for an experiment starting in the initial state indicated. The purity is defined in Eq. 87, from which the solid curves are derived. The dotted lines are an untruncated theory, whereas the solid lines are truncated at a maximum value of $n = n_{\max}$.

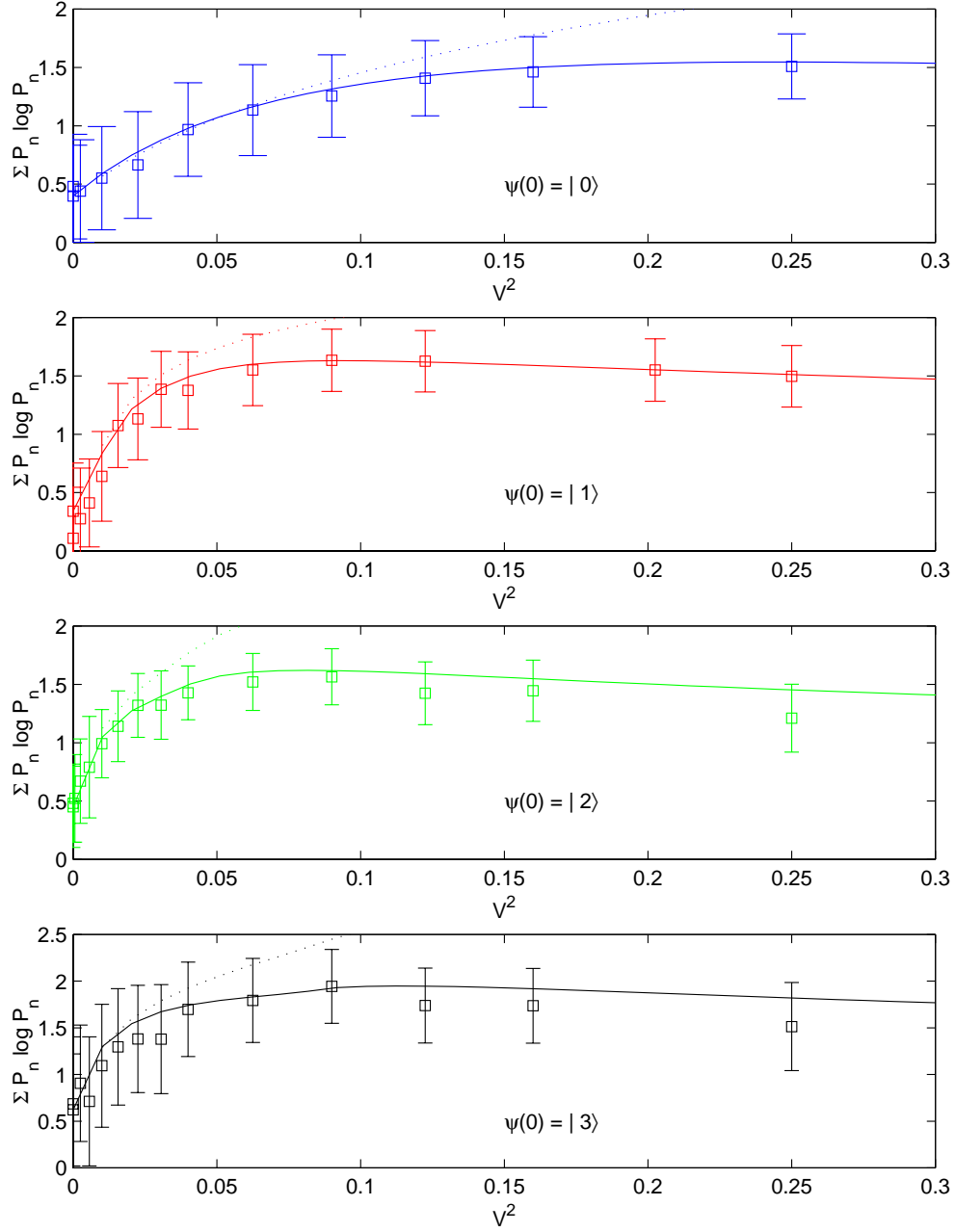


FIG. 17. Evolution of entropy for initial Fock states in hot amplitude reservoir. Each graph shows the time evolution of the entropy of the motional state for an experiment starting in the initial state indicated. The entropy is defined in Eq. 88, from which the solid curves are derived. The dotted lines are an untruncated theory, whereas the solid lines are truncated at a maximum value of $n = n_{\text{max}}$.

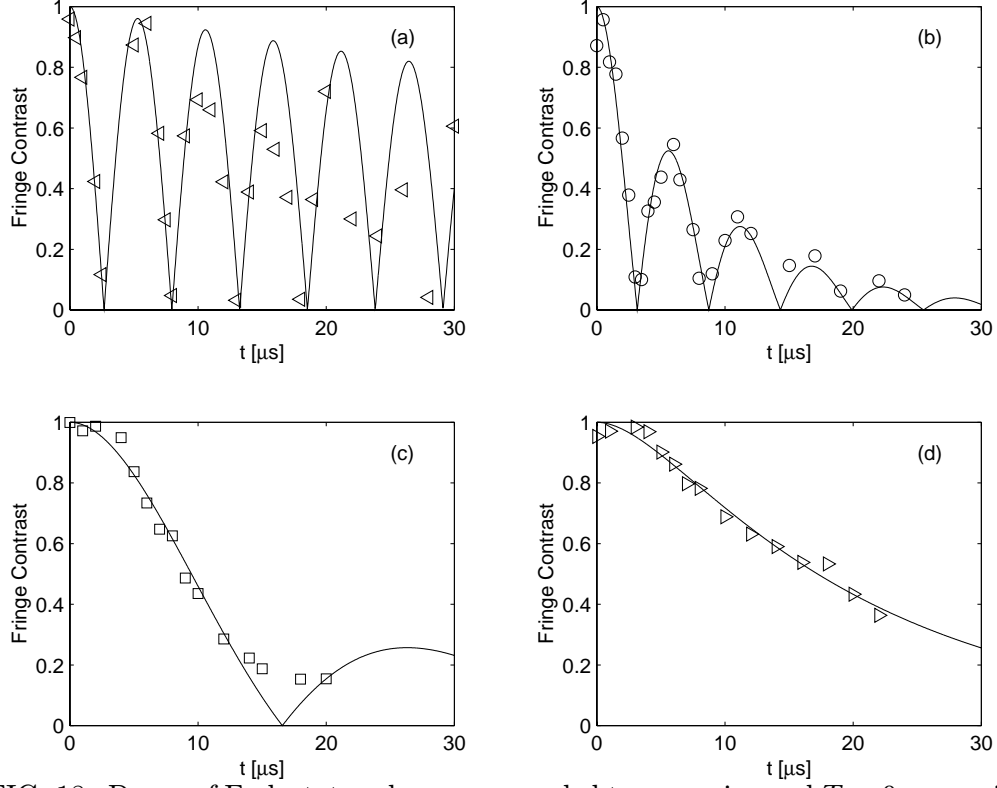


FIG. 18. Decay of Fock state coherences coupled to an engineered $T = 0$ reservoir. The points in each graph are the contrast of a Ramsey fringe which measures the coherence between the $|0\rangle$ and $|2\rangle$ motional states as the time of continuous Raman cooling ($T = 0$ reservoir) is varied. The graphs have progressively larger ratios of $\gamma_{\text{eff}}/\Omega_{\text{rsb}}$, the ratio of the rate of decay to coherent evolution. The Stark-induced detunings are corrected experimentally, that is, the position of the RSB and its drive laser are made coincident. The theory curves are fits to Eq. 80.

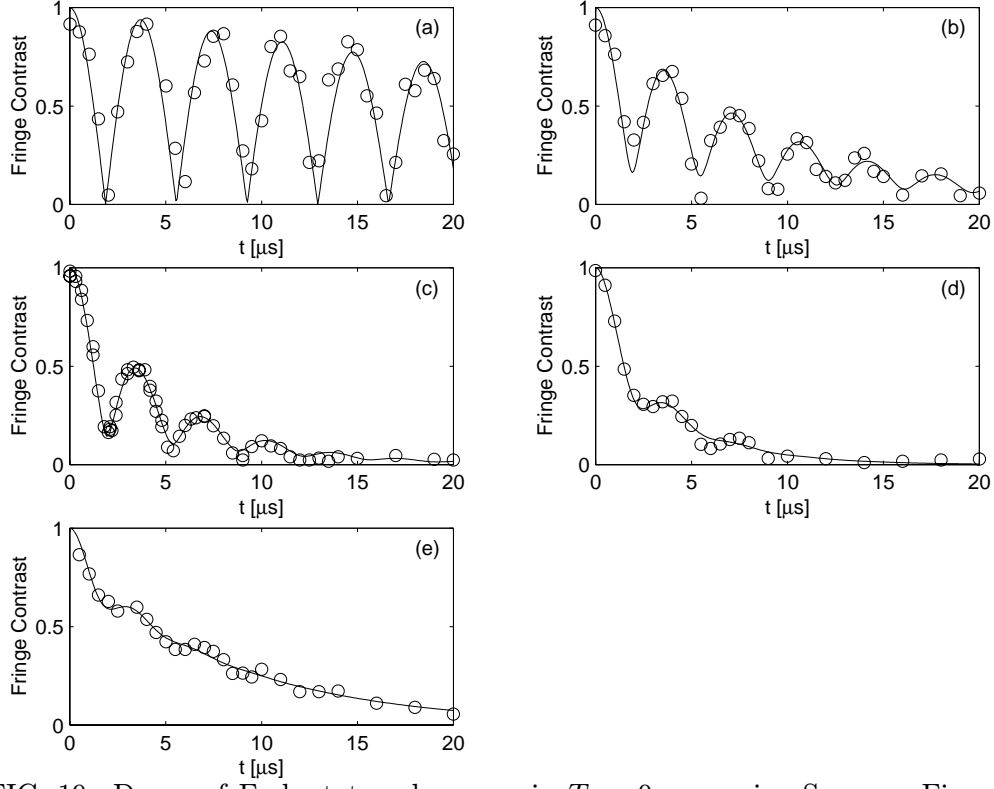


FIG. 19. Decay of Fock state coherences in $T = 0$ reservoir. Same as Figure 18, except the Stark-induced detunings are not corrected experimentally, but are accounted for in the theory curves, which are fits to Eq. 91. See the text for a discussion.

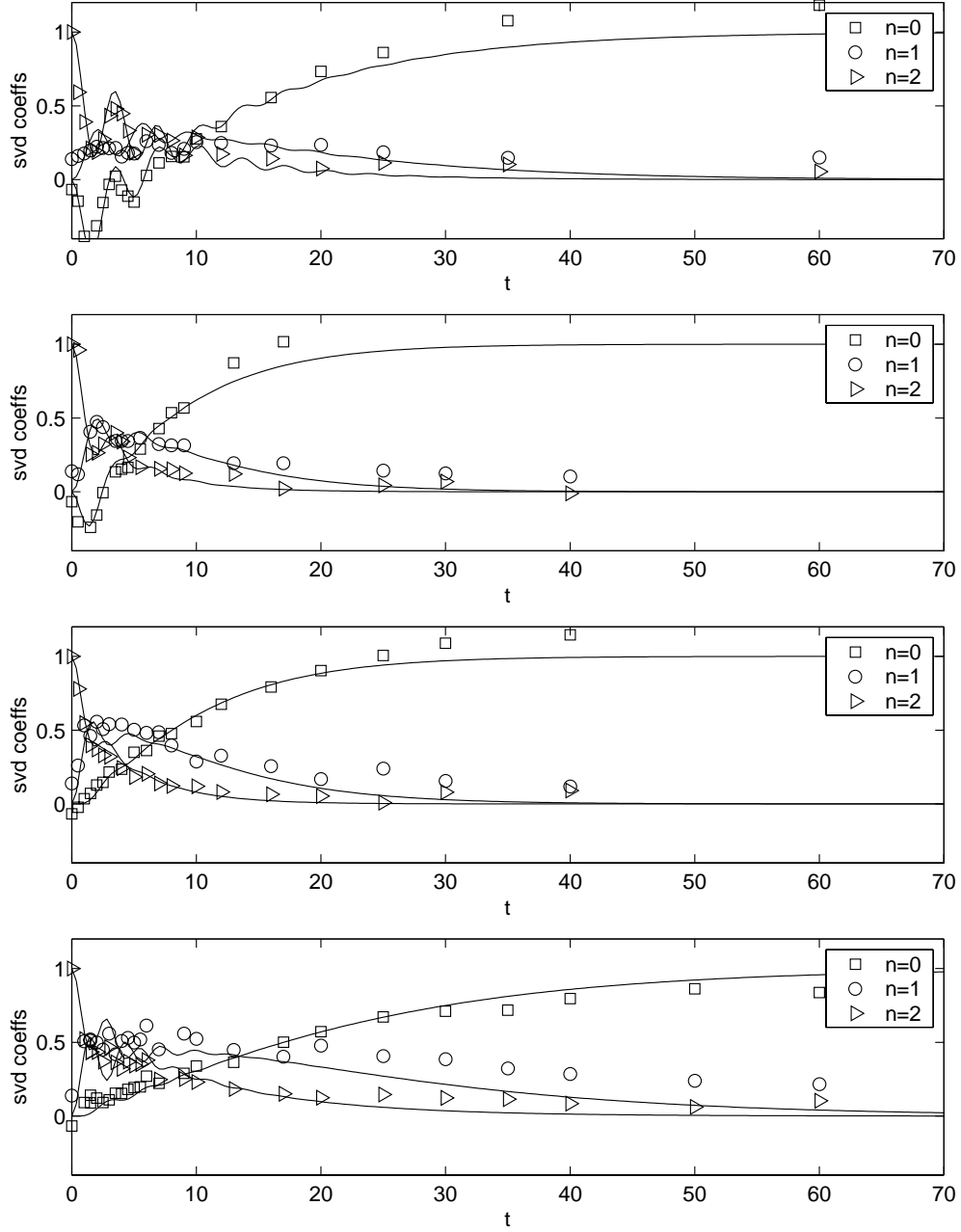


FIG. 20. Decay of Fock state populations in a $T = 0$ reservoir starting from $\psi(0) = |2\rangle$. The strength of the Red Doppler (which provides dissipation) is increased starting from the upper graph. Theory curves are from Eq. 12 with a modification to account for residual population left in $|\uparrow\rangle$ at the end of the continuous cooling cycle. See the text for a discussion.

$\pi/2$ pulse	π pulse	State
carrier	1 st RSB	$ \downarrow\rangle(0\rangle + 1\rangle)/\sqrt{2}$
1 st BSB	1 st RSB	$ \downarrow\rangle(0\rangle + 2\rangle)/\sqrt{2}$
2 nd BSB	1 st RSB	$ \downarrow\rangle(0\rangle + 3\rangle)/\sqrt{2}$
1 st BSB	2 nd BSB	$ \uparrow\rangle(1\rangle + 2\rangle)/\sqrt{2}$

TABLE I. The stimulated Raman pulses required for the first beamsplitter of the Fock state interferometer where the initial state is always $|\downarrow\rangle|0\rangle$. To reverse the superposition in the second beamsplitter, first the π pulse is applied, followed by the $\pi/2$ pulse with a phase added with respect to the first $\pi/2$. RSB and BSB stand for red sideband and blue sideband, respectively.